land

MDPI

Article

Rapid Landslide Detection Following an Extreme Rainfall Event Using Remote Sensing Indices, Synthetic Aperture Radar Imagery, and Probabilistic Methods

Aikaterini-Alexandra Chrysafi [1], Paraskevas Tsangaratos [1,*], Ioanna Ilia [1] and Wei Chen [2]

[1] Laboratory of Engineering Geology and Hydrogeology, Department of Geological Sciences, School of Mining and Metallurgical Engineering, National Technical University of Athens, 15780 Zografou, Greece; alexchrysafi@mail.ntua.gr (A.-A.C.); gilia@metal.ntua.gr (I.I.)
[2] College of Geology and Environment, Xi'an University of Science and Technology, Xi'an 710054, China; chenwei0930@xust.edu.cn
* Correspondence: ptsag@metal.ntua.gr

Abstract: The rapid detection of landslide phenomena that may be triggered by extreme rainfall events is a critical point concerning timely response and the implementation of mitigation measures. The main goal of the present study is to identify susceptible areas by estimating changes in the Normalized Difference Vegetation Index (NDVI), Normalized Difference Moisture Index (NDMI), Bare Soil Index (BSI), and Synthetic Aperture Radar (SAR) amplitude ratio before and after extreme rainfall events. The developed methodology was utilized in a case study of Storm Daniel, which struck central Greece in September 2023, with a focus on the Mount Pelion region on the Pelion Peninsula. Using Google Earth Engine, we processed satellite imagery to calculate these indices, enabling the assessment of vegetation health, soil moisture, and exposed soil areas, which are key indicators of landslide activity. The methodology integrates these indices with a Weight of Evidence (WofE) model, previously developed to identify regions of high and very high landslide susceptibility based on morphological parameters like slope, aspect, plan and profile curvature, and stream power index. Pre- and post-event imagery was analyzed to detect changes in the indices, and the results were then masked to focus only on high and very high susceptibility areas characterized by the WofE model. The outcomes of the study indicate significant changes in NDVI, NDMI, BSI values, and SAR amplitude ratio within the masked areas, suggesting locations where landslides were likely to have occurred due to the extreme rainfall event. This rapid detection technique provides essential data for emergency services and disaster management teams, enabling them to prioritize areas for immediate response and recovery efforts.

Keywords: extreme rainfall; rapid landslide detection; remote sensing indices; landslide susceptibility; weight of evidence

Academic Editor: Faccini Francesco

Received: 8 October 2024
Revised: 5 December 2024
Accepted: 24 December 2024
Published: 26 December 2024

Citation: Chrysafi, A.-A.; Tsangaratos, P.; Ilia, I.; Chen, W. Rapid Landslide Detection Following an Extreme Rainfall Event Using Remote Sensing Indices, Synthetic Aperture Radar Imagery, and Probabilistic Methods. *Land* **2025**, *14*, 21. https://doi.org/10.3390/land14010021

1. Introduction

Landslides are considered one of the most destructive natural hazards, and have been reported to have significant socio-economic disruption, threatening the lives and properties of organized societies worldwide [1,2]. The manifestation of landslides can be triggered by extreme weather events such as heavy rainfall that may influence the hydrological conditions and soil saturation levels, thus affecting the stability of slope surfaces [3–5]. In recent years, the accurate prediction and the necessary implementation of mitigation measures has heighted due to advancements in remote sensing and geospatial analysis techniques [6–9].

Landslides leave a unique mark on the landscape, in most cases creating a visible scar and depositing debris at their base, often changing the drainage patterns and the vegetation cover [10]. Traditional methods of landslide detection typically involve field surveys and visual inspections [11,12]. In earlier years, experienced geomorphologists collected and analyzed landslide-related data through the inspection and interpretation of aerial images, preferably stereoscopic, implementing criteria that refer to characteristics of images such as color, tone, texture, shape, size, and other characteristics related to morphology and structural settings [13–15]. However, although this kind of process could be characterized as direct and detailed, they can be time-consuming and limited by availability of related data. In contrast, advanced remote sensing methods integrate satellite and aerial imagery to detect landslides over large areas [11,14–17]. Techniques such as optical satellite imagery, radar interferometry, and LiDAR technology provide important data concerning changes of the morphology, allowing real-time monitoring, often with higher precision and frequency compared to traditional approaches. Additionally, satellite-derived indices such as the Normalized Difference Vegetation Index (NDVI), Normalized Difference Moisture Index (NDMI), and Bare Soil Index (BSI) enhance the ability to identify potential landslide-prone areas, since they could provide insights into vegetation health, soil moisture, and exposed soil surfaces, which are critical for detecting disturbances in natural landscapes [18–20]. By combining these indices with remote sensing data, it is possible to better predict and manage landslide risks, leading to more effective emergency planning and response [21–24]. In addition to traditional and advanced remote sensing methods, Sentinel-1 (S1) Synthetic Aperture Radar (SAR) data significantly improves landslide detection capabilities. SAR has been a valuable tool in landslide studies for nearly two decades, primarily through interferometric SAR for measuring ground surface deformation [25–31]. Additionally, SAR radar backscatter intensity and coherence-based change detection have proven effective in identifying natural hazards, including landslides [15,32–36].

Notable examples of the approaches described earlier include the work of Mondini et al. [15], which implemented Sentinel-1 SAR C-band images, particularly in areas where optical imagery is limited. The authors reported that from a database of 32 landslide cases, around 84% exhibit changes in SAR amplitude that may be attributed to surface changes caused by landslide phenomena. Similarly, Handwerger et al. [7] developed a cloud-based methodology within Google Earth Engine (GEE) by incorporating multiple SAR images from different acquisition angles and applying topographic masks. In another study, Scheip and Wegmann [37] developed HazMapper, an open-access hazard mapping application utilized through GEE, which calculated the relative difference in the normalized difference vegetation index (rdNDVI), an index that was an indicator for changes in vegetation cover following the occurrence of a natural disaster. Notti et al. [38] developed a two-phase procedure that could detect shallow landslides using Sentinel-2 images. The authors used the NDVI index along with geomorphological characteristics to successfully identify landslides. Phakdimek et al. [20] developed a landslide detection model based on classification and regression tree (CART) using differential spectral indices and amplitude ratio changes. The authors used Sentinel-1 and Sentinel-2 data, achieving moderately good to excellent accuracy. In an analogous study, Peters et al. [39] developed the ML-LaDeCORsat approach for landslide detection, a machine learning-based approach that integrates Sentinel-1, Palsar-2, and Sentinel-2 satellite imagery within GEE that combines optical and radar data.

Despite the well-designed detection approaches that were previously discussed, several limitations are present. In most cases, there are issues concerning false positives, especially in areas of riverbank erosion or cultivated land [38]. In addition, relying on single index approaches using either NDVI, NDMI, or BSI may capture changes on the surface, but may not always correspond to changes due to landslide movements. On the

other hand, radar-based methods can be less effective in correctly classifying types of surface changes without additional context from optical or multispectral data [15].

In this context, to overcome these limitations, our methodological approach developed partly in the GEE platform, combining indices derived by optical and radar data analysis. Specifically, NDVI, NDMI, and BSI indices were calculated to analyze the vegetation health, soil moisture, and exposed soil conditions before and after an extreme rainfall incidence, whereas an SAR amplitude-based change detection ratio was calculated to indicate significant changes in ground surface properties. This formed the Rapid landslide Detection (RLD). In addition, to avoid false positives, we developed a landslide susceptibility model based on the Weight of Evidence (WofE) method. Our methodology uses a similar approach to the approaches of Adriano et al. [40] and Handwerger et al. [7], who applied an SAR backscatter change detection approach. The researchers reported enhanced performance when integrating a DEM (Digital Elevation Model) mask, and similarly, when land cover data were used to filter out areas where landslides were less likely to occur. In line with these studies, we applied the WofE models using geomorphological variables and a set of historical landslides. The WofE model, which calculates the likelihood ratio for landslides, assisted in indicating the most prone areas, which, when combined with the previous phase of analysis, gave the final characterization of the investigated area and specifically the identification of potential landslides. This resulted in the creation of the Rapid Landslide Detection-WofE (RLD-WofE) model. Additionally, we applied a topographic masking approach by excluding areas with slope angles less than 15 degrees, forming the Rapid Landslide Detection-Slope (RLD-Slope) model [38].

The novelty of our study lies in the integrated approach that combines empirical data from remote sensing with model-based predictions using the WofE model. Leveraging the advantages of optical and radar data analysis, our methodology effectively detects landslides, while using the WofE landslide susceptibility model to minimize false positives, thus enhancing the accuracy and reliability of the developed approach. Designed as a rapid tool for landslide inventory mapping, the approach offers reliable and efficient detection capabilities, essential to support emergency response agencies in disaster scenarios. To verify the effectiveness of the methodology, it was applied to the specific case of Storm Daniel, which struck central Greece in September of 2023, particularly affecting the study area of Mount Pelion, located on the Pelion Peninsula.

2. Materials and Methods

In this study, we adopted a systematic approach, combining the analysis of remote sensing data with geospatial modeling to enhance the detection of landslide phenomena that were triggered by an extreme rainfall event. The main investigation tools for the implementation of the methodology were the GEE platform and the ArcGIS suite (version 10.5). GEE is considered an advanced cloud-based platform, which provides free access to a vast multi-petabyte archive of geospatial datasets, also including weather, climate data, and digital elevation models, covering over four decades of historical and contemporary Earth observation imagery [33,41]. Concerning the ArcGIS suite, it is one of the most powerful tools for modeling landslide susceptibility and hazard assessments [42]. Using geoprocessing tools such as the Weighted Overlay and the Raster Calculator, the GIS-based models can effectively predict areas of high landslide susceptibility [43]. GEE was utilized for the pre- and post-event analysis of the various remote sensing indices, while ArcGIS was used to implement the WofE model and provide the final inventory map based on the integration of the remote sensing indices and the high and very high susceptible areas. The methodology involves five key phases of analysis, data acquisition, preprocessing, index

calculation, susceptibility modeling, and detection and validation, which are described in detail below (Figure 1).

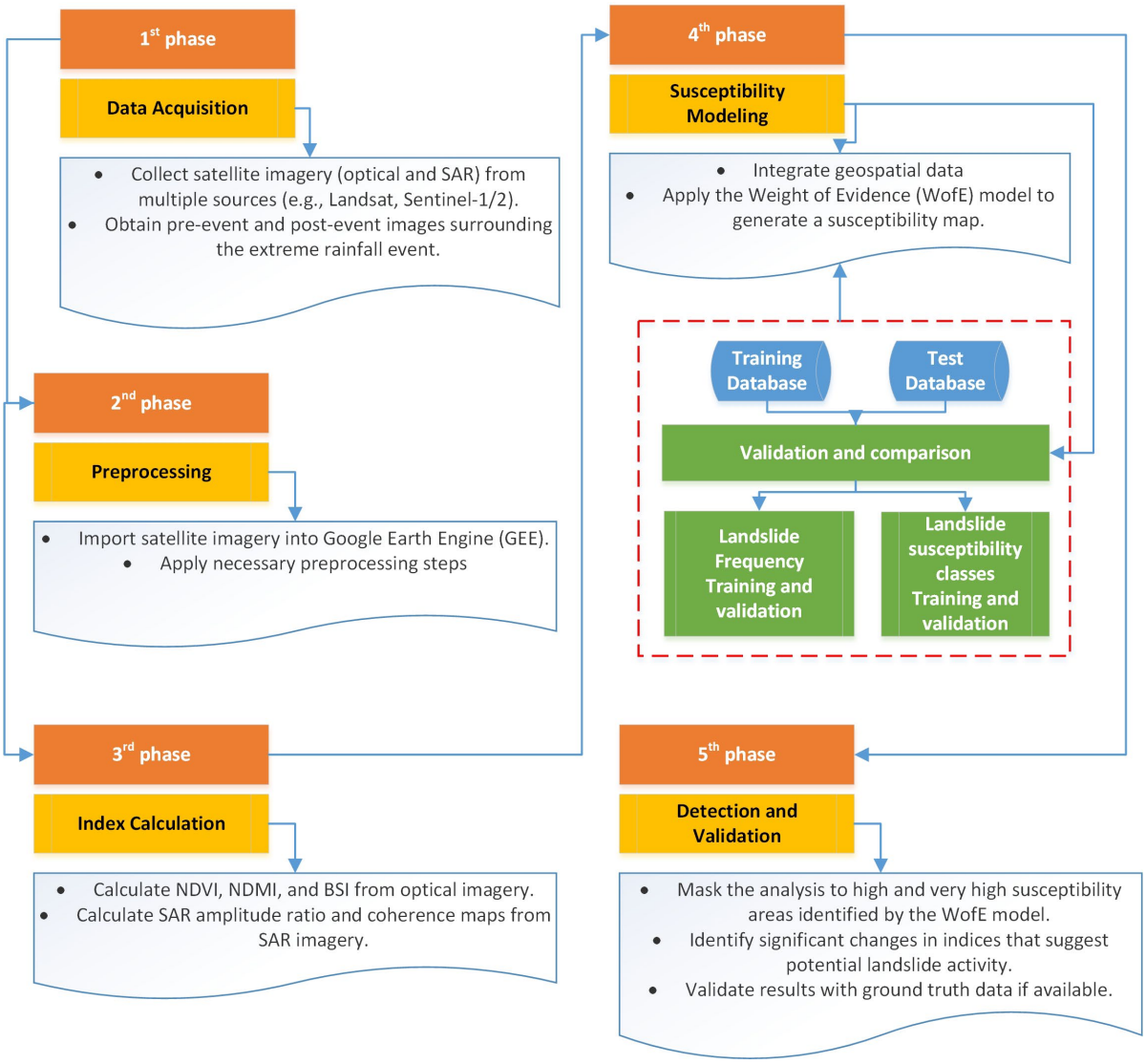

Figure 1. Flowchart of the developed methodology.

2.1. Data Acquisition

The first phase involved collecting pre-event and post-event optical satellite imagery and SAR Imagery. SAR amplitude data are obtained from the Copernicus Sentinel-1 satellite constellation. The Sentinel-1 satellites is equipped with a C-band radar sensor, which operates at a wavelength of 5.6 cm, having a minimum revisit time of 12 days for a specific area. In GEE, Ground Range Detected (GRD) images have been subjected to several preprocessing steps, including thermal noise removal, radiometric distortion correction, and terrain effects correction. For the last process digital elevation data from the Shuttle Radar Topography Mission has been used [20]. GRD images are provided at a spatial resolution of 10 m and support up to four polarization configurations: 1. a vertical transmit/vertical receive (VV), 2. a horizontal transmit/horizontal receive (HH), 3. a vertical transmit/horizontal receive (VV + VH), and 4. a horizontal transmit/vertical receive (HH + HV) (Table 1). For our study, we utilized SAR data in the VH polarization mode that appears more sensitive to forest biomass structure, thus making them effective for identifying landslides in vegetated areas [44].

Table 1. Sentinel-1 data.

Spectral Band	Polarization	Central Frequency (GHz)	Spatial Resolution (m)
C-band	VV	5.405	10
C-band	VH	5.405	10
C-band	HH	5.405	10
C-band	HV	5.405	10

Additionally, multi-spectral satellite imagery from Sentinel-2 sensors was used to calculate the NDVI, NDMI, and BSI indices. The Sentinel-2 images analyzed included 13 spectral bands at varying spatial resolutions, ranging from 10 m for visible and near-infrared bands to 20 m for red edge and shortwave infrared bands (Table 2).

Table 2. Sentinel-2A and 2B data.

Spectral Band	Band	Wavelength (μm)	Spatial Resolution (m)
Blue (B)	B2	0.46–0.52	10
Green (G)	B3	0.54–0.58	10
Red (R)	B4	0.65–0.68	10
Red edge (RE1)	B5	0.698–0.712	20
Red edge (RE2)	B6	0.733–0.747	20
Red edge (RE3)	B7	0.773–0.793	20
Near-infrared (NIR)	B8	0.784–0.9	10
Near-infrared (NIR)	B8A	0.855–0.875	20
Shortwave infrared (SWIR1)	B11	1.565–1.655	20
Shortwave Infrared (SWIR2)	B12	2.1–2.28	20

To assess the impact of the rainfall event on vegetation and potential landslide areas, we defined specific time periods for analysis. The pre-event period was set from 1 August 2023, to 1 September 2023, allowing for baseline data collection prior to the extreme rainfall event. During this time, we utilized the Sentinel-1 and Sentinel-2 data to capture the vegetative health and moisture content before the onset of significant precipitation. For the pre-event analysis, 5 Sentinel-1 images and 12 Sentinel-2 were analyzed.

Following the extreme weather event, we established the post-event period from 10 September 2023, to 30 October 2023. This interval was critical for analyzing the immediate effects of the rainfall on the landscape and monitoring changes in vegetation indices, particularly NDVI, NDMI, and BSI, as well as alterations in the forest biomass structure identified through the VH polarization mode of the SAR data. For the post-event analysis, 8 Sentinel-1 images and 20 Sentinel-2 were analyzed.

While the Sentinel-1 and Sentinel-2 dataset imagery are widely used in studies that focus on landslide detection and spatial landslide prediction, each serves different purposes. The Sentinel-1 imagery, which is used to calculate the SAR amplitude ratio, is effective in detecting surface changes under all-weather and day–night conditions, making it ideal for radar-based analyses. In contrast, Sentinel-2 provides multispectral visual imagery, which is not suitable for SAR amplitude ratio, but excels in calculating vegetation and soil indices such as NDVI, NDMI, and BSI. By integrating these datasets, our approach leverages their complementary advantages to enhance accuracy and reduce false positives in post-event landslide detection.

2.2. Data Preprocessing

The second phase involved preprocessing the optical imagery and preprocessing the SAR imagery. Stacked NDVI images are used instead of just one image for the pre-event and post-event periods because they provide a more robust and accurate representation of vegetation conditions over time. Using multiple images allows researchers to account for natural variability in vegetation due to daily or seasonal changes, as well as other factors like cloud cover, sensor noise, or slight differences in illumination. A single image might capture an anomaly or short-term fluctuation that does not accurately represent the overall vegetation health before or after the event. Stacking multiple images smooths out these variations, creating a more reliable "mean" NDVI value that reflects typical conditions. This approach also improves the detection of subtle changes caused by the event, like landslides, by ensuring that the comparisons are made against a stable baseline rather than a potentially unrepresentative snapshot.

In the present study, Sentinel-1 GRD images acquired in the VV polarizations were employed, which in GEE are already preprocessed. The preprocessing in GEE involves removing thermal noise, applying radiometric calibration, and terrain correction using the Shuttle Radar Topography Mission DEM [45]. In our case, the images were further preprocessed with a 7×7 adaptive Sigma Lee speckle filter implemented in the GEE platform to reduce the granular noise [46].

2.3. Calculation of Indices

In the third phase of the rapid landslide detection approach, several critical remote sensing indices are calculated from optical imagery to facilitate change detection and identify significant environmental changes between pre-event and post-event conditions [39]. This involves calculating the NDVI to assess vegetation health, the NDWI to evaluate water content, and the BSI to detect changes in exposed surface properties.

2.3.1. Normalized Difference Vegetation Index (NDVI)

The NDVI index is used to assess the health of vegetation, with values typically ranging from -1 to 1. Healthy vegetation absorbs a significant percentage of visible light and reflects high amounts of light in the near-infrared spectrum. In contrast, sparse or unhealthy vegetation is characterized by increased reflectance in the visible spectrum and reduced reflectance in the near-infrared [47]. In the context of an extreme rainfall event, pre- and post-event NDVI calculations can be highly effective in detecting landslides and their impacts on vegetation. Prior to the event, NDVI values can indicate the normal vegetation health in the area, with dense, healthy vegetation typically showing high values (0.6 to 0.9). After the rainfall, a significant landslide would likely cause vegetation to be stripped away, exposing bare soil or rock, leading to much lower NDVI values (0.1 or below). By comparing the pre-event and post-event NDVI images, researchers can identify areas where drastic reductions in NDVI values have occurred, signaling potential landslide locations. Additionally, by analyzing NDVI changes over time, the recovery of vegetation in the affected areas can be monitored, providing insight into the long-term ecological impacts of the landslide.

We used the Sentinel-2 band of *NIR* and *Red*, and the following equation to calculate the index [48] (Equation (1)):

$$NDVI = \frac{(NIR - Red)}{(NIR + Red)} \quad (1)$$

where *NIR* is the near-infrared light reflected by vegetation, and *Red* is the visible light absorbed by vegetation. To detect any changes in the research area caused by the manifes-

tation of the extreme rainfall event, a simple abstraction between the pre-event stacked Sentinel-2 bands and the post-event stacked Sentinel-2 bands were applied based on the following equation (Equation (2)):

$$NDVI_{chn} = NDVI_{pre} - NDVI_{post} \quad (2)$$

A significant negative change in *NDVI* values corresponds to vegetation removal, which may be attributed to landslide activity, especially after extreme rainfall events. On the other hand, positive or no change assume than no significant disturbance on vegetation cover has been manifest during the extreme rainfall event [49].

2.3.2. Normalized Difference Moisture Index (NDMI)

This index assists in identifying the moisture content in vegetation cover, which can be an indicator of the presence of soil saturation—a precursor to many landslide events [50]. The estimation of NDMI is based on the following equation [51] (Equation (3)):

$$NDMI = \frac{(NIR - SWIR)}{(NIR + SWIR)} \quad (3)$$

where *NIR* is the near-infrared light reflected by vegetation, and *SWIR* is the short-wave infrared light, which increases in reflection with moisture content.

$$NDMI_{chn} = NDMI_{pre} - NDMI_{post} \quad (4)$$

A negative change, a decrease in the post-event *NDMI* index, in most cases indicates an area where the vegetation cover has been removed, exposing bare soil or bedrock, thus retaining less moisture. However, in some cases, a positive change might happen in areas associated with landslide phenomena, in which landslides deposits earth material in low-lying areas or in areas where debris may block the water flow [52].

2.3.3. Bare Soil Index (BSI)

The BSI is a remote sensing index used to detect changes in areas of exposed soil, which is very important in monitoring environmental settings such as landslides, soil erosion, and areas at risk of degradation due to the absence of vegetation. The following equation is used to estimate the BSI [53] (Equation (5)):

$$BSI = \frac{(SWIR + Red) - (NIR + Blue)}{(SWIR + Red) + (NIR + Blue)} \quad (5)$$

where *Red* is visible red reflectance, *NIR* is the near-infrared, and *SWIR* is the short-wave infrared band, which are sensitive to soil and vegetation conditions (Equation (6)).

$$BSI_{chn} = BSI_{pre} - BSI_{post} \quad (6)$$

A positive change in the *BSI* index indicates an increase in the bare soil surface that may be associated with landslide areas. On the other hand, a negative change may be attributed to the process of deposition, in which landslide material may be deposited.

2.3.4. SAR Amplitude Change

Amplitude in SAR data is calculated based on the radar backscatter intensity, which represents the strength of the radar signal reflected to the satellite. SAR sends microwave pulses to the Earth's surface, and the amplitude of the returned signal is influenced by the

surface's characteristics, such as its roughness, geometry, and dielectric properties [20]. The amplitude can be calculated using the following formula (Equation (7)):

$$A = \sqrt{I} \tag{7}$$

where A is the amplitude, and I is the intensity of the backscattered signal. In GEE, the backscatter values are stored as the SAR intensity in the 'VV' or 'VH' band.

Concerning the identification of potential landslides using amplitude, this could be feasible if we calculate changes in amplitude, defined as the difference between the pre-event and the post-event amplitude. Since GEE provides amplitude data in decibels (dB), this is equivalent to the amplitude ratio approach [20] (Equation (8)):

$$A_{chn} = \log_{10} \frac{A_{pre}}{A_{post}} \tag{8}$$

Positive values of A_{chn} indicate a decrease in SAR amplitude recorded after a landslide event. This is due to the significant changes that a landslide causes in the surface properties of the soil, affecting radar reflectivity, slope geometry, surface roughness, and dielectric properties [36,40].

2.4. Landslide Detection and Landslide Susceptibility Mapping

The fourth phase of analysis involved two procedures: the first procedure included the production of a landslide detection map based on the three indices ($NDVI_{chn}$, $NDWI_{chn}$, BSI_{chn}) and the SAR amplitude change, and the second procedure included the generation of the landslide susceptibility map based on the historical landslides and geomorphological settings using the WofE model. For the first procedure, the features $NDVI_{chn}$, $NDWI_{chn}$, BSI_{chn}, and the SAR amplitude change were normalized within the range of 0 to 1 to ensure consistent processing, using the min–max normalization algorithm [54] (Equation (9)).

$$x_{new} = \frac{x - x_{min}}{x_{max} - x_{min}} \tag{9}$$

These normalized values were then aggregated to produce a single raster output, which was subsequently reclassified into five classes of landslide detection potential using a Natural Break classification scheme [55]. For the second procedure, the landslide susceptibility map was created. Landslide susceptibility refers to the likelihood of landslide occurrence in a specific area, and is influenced by a complex interplay of factors, including terrain, lithology, climate, human activity, and environmental conditions [56,57]. As has been stated by many researchers, the choice of control factors for modeling landslide susceptibility is largely dictated by local morphological and geological settings [58,59]. However, despite the extensive research conducted in this topic, a standardized method for choosing these factors remains not clearly formed [60,61], as the influential factors can vary significantly from one region to another region. To enhance the prediction accuracy of landslide susceptibility models, it is very important to carry out optimization work to evaluate the contribution and correlation of various conditioning factors through quantitative indicators [62].

2.4.1. Landslide-Related Variables

To assess the study area's susceptibility to landslides, five variables were selected, considering both the local geoenvironmental conditions and available database. These variables include altitude, which influences terrain impact, precipitation patterns, and vegetation cover [63], aspect, affecting solar radiation, evaporation, weathering, vegetation,

and slope erosion [64], and slope, a critical factor in stress distribution and soil sliding potential [65]. Additionally, two curvature variables, the plan curvature, which measures the horizontal surface curvature [66], and the profile curvature, which indicates the vertical elevation changes [67], are also used in the present analysis. The stream power index (SPI) assesses erosion and water flow energy [68–70]. In most landslide susceptibility assessments, lithology or geological composition is considered a significant factor due to its influence on the stability of terrain and soil properties [1]. Different rock types can exhibit varying degrees of susceptibility to weathering, erosion, and water infiltration, all of which contribute to landslide potential [71]. However, in this particular study, we have excluded lithology as a variable because the research area is predominantly composed of a single geological formation—ortho- and para-metamorphic rocks—as further discussed in Section 3. Additionally, the available geological map, at a scale of 1:50,000, does not further differentiate within this formation, making it difficult to account for any subtle geological variations. The homogeneity of this geological setting means that lithological variations do not play a significant role in influencing landslide susceptibility in the area. Since there is little to no variability in rock types across the region, including lithology as a factor would offer minimal additional insights into the susceptibility analysis. Therefore, focusing on other factors, such as terrain, slope, aspect, and curvature, which exhibit more variability across the study area, allows for a more effective and targeted analysis.

2.4.2. Weight of Evidence (WofE)

The Weight of Evidence (WofE) method is a probabilistic method initially developed in the 1980s for mapping mineral potential by combining multiple lines of evidence to support a given hypothesis [72,73]. Although originally designed for non-spatial applications, the method is now applied to spatial predictions, and especially in cases where the goal is to estimate the probability of point occurrences [72]. Regarding its application to landslide-related analyses, the method has been widely used, particularly through the integration of GIS technology in numerous studies [74,75]. According to Neuhauser et al. [76], the WofE method is effective in analyzing the spatial distribution of landslides, as well as in the ability to extract quantitative spatial information, which can be used to determine the influence of various factors related to the occurrence of landslides. Both continuous and categorical factors can be used in the application of the method, which, in the process, form distinct categories to which a unique weight of evidential values is assigned. The method assumes conditional independence between the variables and requires that the distribution of the data for each variable follows a normal distribution. It is important to test for conditional independence to exclude dependent variables that could bias the results due to double counting of their effects on the results. This process is particularly critical when selecting variables for landslide susceptibility, hazard, and risk analyses [77]. The WofE method is rooted in the principles of Bayes' theorem, and employs the concepts of prior and posterior probability to statistically evaluate the relative influence of evidential variables [78]. In this context, the method assesses whether a set of independent variables can trigger landslides by analyzing the spatial correlation between the distribution of historical landslide occurrences and the distribution of susceptibility variables. It quantifies the degree of influence each variable has on past events and its potential impact on future landslide occurrences [79]. In the case under consideration, a simple application of Bayes' theorem was used through the binary map method. This approach evaluates the presence or absence of a landslide event, and determines the degree of influence for each variable [80]. The method calculates the prior probability by determining the total number of landslides observed in the past under specific conditions or within different classes of each variable, divided by the total area corresponding to each class. The WofE method's effectiveness

is measured through the contrast magnitude, C, which indicates the spatial association between landslide events and evidence layers. In particular, a positive contrast value indicates a strong positive correlation, while a negative contrast value means a negative spatial correlation [80]. The following equations are used to estimate the weights of each variable (Equations (10)–(12)):

$$W_{ji}^{+} = \ln \frac{P(V|L)}{P(V|\overline{L})} \tag{10}$$

$$W_{ji}^{-} = \ln \frac{P(\overline{V}|L)}{P(\overline{V}|\overline{L})} \tag{11}$$

$$C_{ji} = W_{ji}^{+} - W_{ji}^{-} \tag{12}$$

where L represents the amount of landslide grid cells in the i^{th} class of the j^{th} landslide variable, and $\overline{L}$ is the number of non-landslide grid cells in the i^{th} class of the j^{th} landslide variable. $P(V|L)$ and $P(V|\overline{L})$ refer to the amount of grid cells in which the landslide-related variables exists in L and in $\overline{L}$, whereas $P(\overline{V}|L)$ and $P(\overline{V}|\overline{L})$ refer to the amount of grid cells in which the landslide-related variables do not exist in L and in $\overline{L}$.

For a given grid cell, the final landslide susceptibility value is calculated as the sum of the total contrast values in all categories of the evidence variables (Equation (13)):

$$LSI = \sum_{j=1}^{n} \sum_{i=1}^{m} C_{ji} \tag{13}$$

where j refers to each landslide-related variable and i represents the class of each landslide-related variable. A higher value of LSI indicates that the grid cell is more susceptible to landslides based on the evidence factors considered.

2.4.3. Training and Validation Database

The training and validation of landslide susceptibility models requires a robust and comprehensive database to ensure accurate predictions. For this purpose, a dataset comprising approximately 180 recorded landslides from past events has been utilized. This historical landslide inventory serves as the foundation for training the models, allowing them to learn the patterns and factors associated with landslide occurrences. The database is divided into two subsets: one for training and the other for validation [81]. The training subset, 70% of the total number of historical landslides, was used to develop and calibrate the model. The validation subset, the remaining 30%, was used to test the model's predictive accuracy.

2.4.4. Validation of WofE Model

The validation was carried out by estimating the cumulative portion of observed landslide events within the produced landslide susceptibility classes, and secondly, the estimation of success and prediction rate. In more detail, it has been reported that an effective landslide susceptibility map should display an increase in the landslide density ratio from lower to higher susceptibility classes, while also meeting two key spatial effectiveness criteria [82–84]: the identified landslide-prone areas should predominantly fall within the high susceptibility class, and the high susceptibility class should occupy a relatively small portion of the total area [85,86].

2.5. Landslide Detection and Validation

In the detection and validation phase, the objective was to identify significant changes in the remote sensing indices that indicate potential landslide activity, and validate these

findings with ground truth data obtained from extensive field surveys conducted in December 2023. The final detection maps were produced by combining two previous products: the landslide detection map based on NDVI, NMDI, BSI, and SAR data and the RLD model, and the landslide susceptibility map produced by the WofE model. For the latter, only the high and very high susceptibility zones were utilized to minimize false positives. Additionally, a topographic masking technique was implemented, excluding areas with slope angles less than 15 degrees. This process, combined with the landslide detection map, resulted in the creation of the RLD-Slope model, offering an alternative approach to refine the detection of potential landslides. The analysis was specifically focused on a 50 m buffer zone around the road network. This approach was chosen because our field investigations were conducted along the road, making the surrounding area highly relevant for evaluating landslide occurrences. By concentrating on this buffer zone, we could more accurately assess the performance of the methodology in detecting landslides near the road, where such events pose the greatest risk to critical infrastructure and can cause significant disruption. The validation for this output was based on the landslide density ratio, as discussed earlier, to ensure that the methodology accurately reflects landslide-prone areas. By focusing on the landslide density ratio, we aimed to assess whether the detected landslides, both from remote sensing and ground surveys, predominantly occur within the high and very high susceptibility zones. This approach was taken to verify that the model not only identifies landslide-prone areas effectively, but also minimizes false positives in less susceptible regions. For the overall validation of the methodology, two additional statistical processes were conducted: a receiver operating characteristic (ROC) curve analysis, and a comparison between the RLD, the RLD-Slope, and RLD-WofE models to determine the presence of statistically significant differences. The ROC curve and the area under the curve (AUC) are widely recognized as standard techniques for assessing the performance of predictive models using training and validation datasets [87]. To ensure a balanced dataset for this analysis, an equal number of non-landslide points were randomly generated using the "Create Random Points" geoprocessing tool available in the Data Management Tools of the ArcGIS platform [88]. These points served as a counterpart to the field-identified landslide locations, providing the necessary balance for robust statistical evaluation of the models. Additionally, performance metrics such as precision, recall, and F1-score were used to validate the effectiveness of the models in detecting landslides. Precision, also referred to as the positive predictive value, represents the proportion of correctly identified landslides (true positives) among all instances predicted as landslides. It highlights the model's ability to minimize false alarms in landslide detection. Recall, also known as sensitivity, measures the proportion of actual landslides that were correctly identified by the model, demonstrating its capacity to detect landslides comprehensively. The F1-score, which is the harmonic mean of precision and recall, provides a single metric to assess the balance between reducing false positives and maximizing accurate detection [89].

3. Study Area

3.1. General Setting

The study area is located in the southeastern part of Thessaly, in central Greece, and specifically concerns Mount Pelion, on the Pelion peninsula, which extends between the Aegean Sea and the Pagasetic Gulf (Figure 2). Most of the study area is part of the Municipality of Zagora–Mouresi, covering an area of approximately 108 km^2.

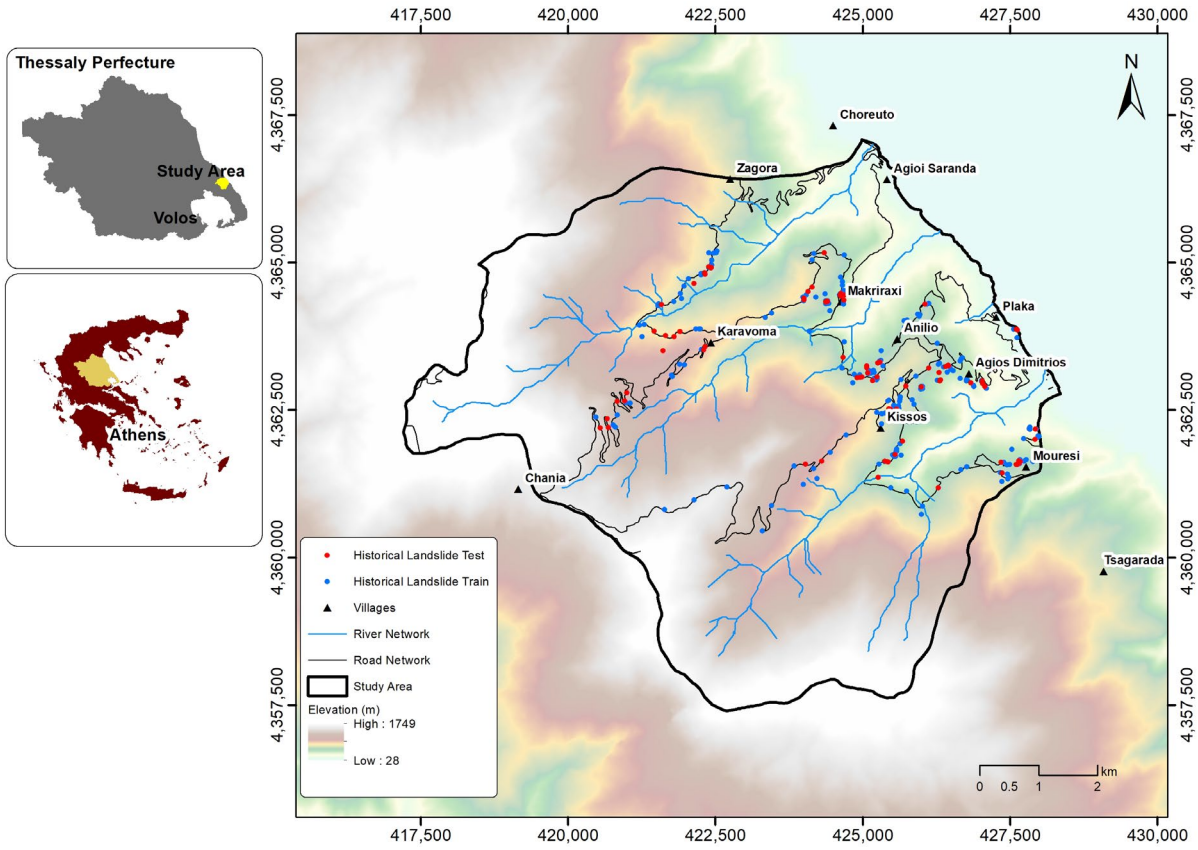

Figure 2. Study area and historical landslides (training and test subsets).

Based on the Thornthwaite climate classification, [90] the area is characterized as semi-arid climate with moderate winter water surplus and mesothermal conditions, with evapotranspiration between 855 mm and 997 mm. This type is typical of areas far from the coast, resulting in a neutral thermal climate. In more detail, Magnesia's climate varies due to its geography and topography. Microclimates are influenced by the rugged terrain and strong Aegean winds. In northern and eastern Pelion, the climate ranges from marine to mountainous, with higher annual rainfall, higher relative humidity, lower average temperatures, and prevailing northern winds. Snowfall is common in mountainous areas, and frosts, though rare, occur from December to March, peaking in January. Annual rainfall averages between 466.8 mm and 793.2 mm.

Concerning the geological settings, the study area is located within the Pelagonian zone and is characterized by a diverse range of formations, spanning from the Quaternary Holocene to the Neo Paleozoic and Triassic periods [91] (Figure 3). The Quaternary Holocene formations include alluvial and fluvial deposits, predominantly consisting of sandy-clay materials interspersed with unconsolidated gravels and pebbles. These gravels and pebbles are primarily composed of schists, with a smaller proportion of limestones. Unconsolidated materials of sand and pebbles are prevalent in the beds of torrents, as well as in small terraces and coastal formations. They cover only a very small portion of the study area, with limited instability problems. The Tertiary Neogene period is represented by acid vein intrusions, comprising a variety of rock types such as quartz, dioritic porphyrites, syenodioritic porphyrites, gabbroporphyrites, dacites, and diabases. These formations add to the region's geological complexity; however, limited instability problems are associated with their presence. The older Neo Paleozoic to lower and middle Triassic systems consist of a range of ortho- and para-metamorphic rocks that have undergone similar metamorphic facies as the eohellenic tectonic nappe. These formations predominantly

include mica- and amphibole-bearing schists such as glaucophane schists, cal-epidote and quartz schists, muscovite, and chlorite schist gneisses, as well as prasinite, quartzites, and phyllites. The western part of the area is particularly rich in glaucophane schists. The micas found in these rocks include muscovite, phengite, and hydromuscovite, with less biotite, while feldspars such as orthoclase and acid plagioclases are also present. Amphiboles, including glaucophane and actinolite, are notable components of the metamorphic assemblage. They are intruded by tertiary acid vein intrusions, and in the upper members of the neo Paleozoic-lower-middle Triassic formations, intercalations of thick-bedded, coarse crystalline marbles (mr) locally occur, white to white-grey in color [91]. Almost all historical landslides are reported within this formation that occupies over 90% of the research area.

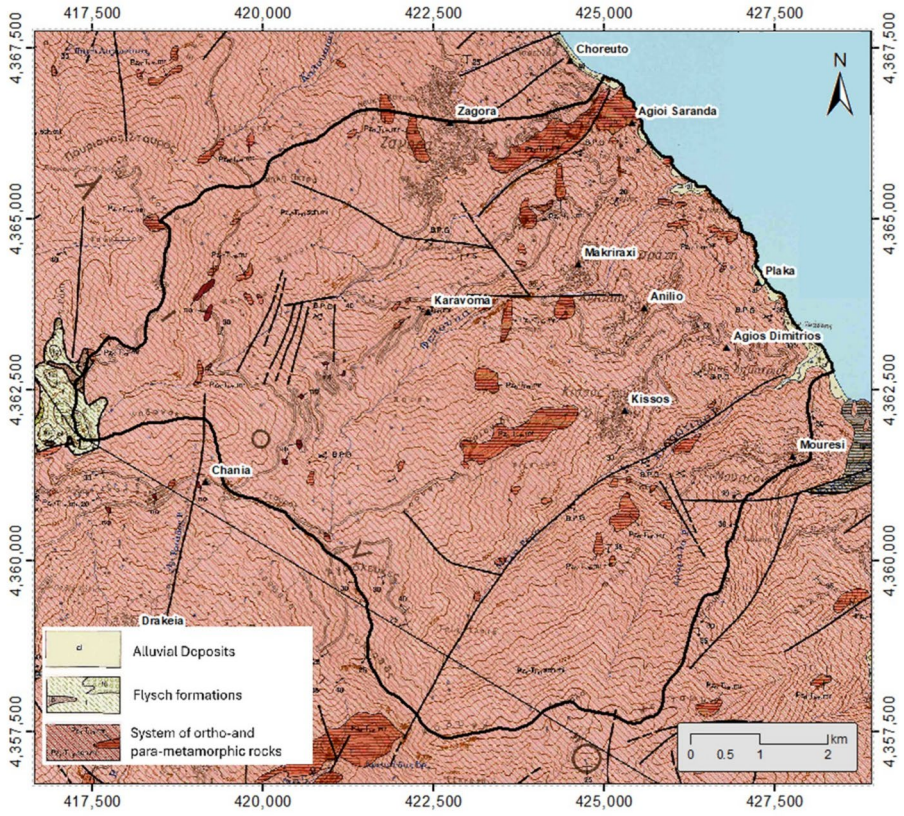

Figure 3. Geological map, adopted by [92].

3.2. Rainstorm Daniel

Regarding the extreme rainfall event that impacted the wider study area, Storm Daniel struck the Mediterranean between 3 September and 8 September 2023. Storm Daniel brought unprecedented rainfall to central Greece, following a period of drought, wildfires, and heatwaves during the Summer. Areas received around 500 mm of rain in just one day, significantly exceeding the average September rainfall and setting new records [93]. The extreme weather led to severe flooding, with massive damage to infrastructure, destruction of buildings and bridges, and entire villages submerged. This event is considered Greece's worst rainfall occurrence on record and the deadliest weather event of the year, with casualties in Greece and neighboring Bulgaria and Turkey. The flooding caused damages amounting to billions of euros, prompting the European Union to allocate EUR 2.25 billion for Greece's recovery efforts.

The following Figure 4a–f shows the rainfall intensity and spatial distribution in Greece, based on the GPM IMERG V06 dataset. The dataset is filtered to a 30 min interval, and includes precipitation estimates that are refined as more data becomes available.

Specifically, maximum precipitation values were selected, and areas with low precipitation (values below 0.5 mm/h) were masked out to highlight significant rainfall events [94]. The Global Precipitation Measurement (GPM) mission is an international satellite initiative designed to provide global-scale observations of precipitation and snowfall at three-hour intervals. The Integrated Multi-Satellite Retrievals for GPM (IMERG) algorithm is a comprehensive methodology that combines data from all passive-microwave instruments in the GPM constellation. The algorithm intercalates, fuses, and interpolates satellite microwave precipitation estimates, while incorporating calibrated infrared (IR) data, rain gauge analyses, and potentially additional sources of precipitation estimates. This process covers the Tropical Rainfall Measuring Mission (TRMM) and GPM eras, providing fine-scale time and space precipitation data globally [94].

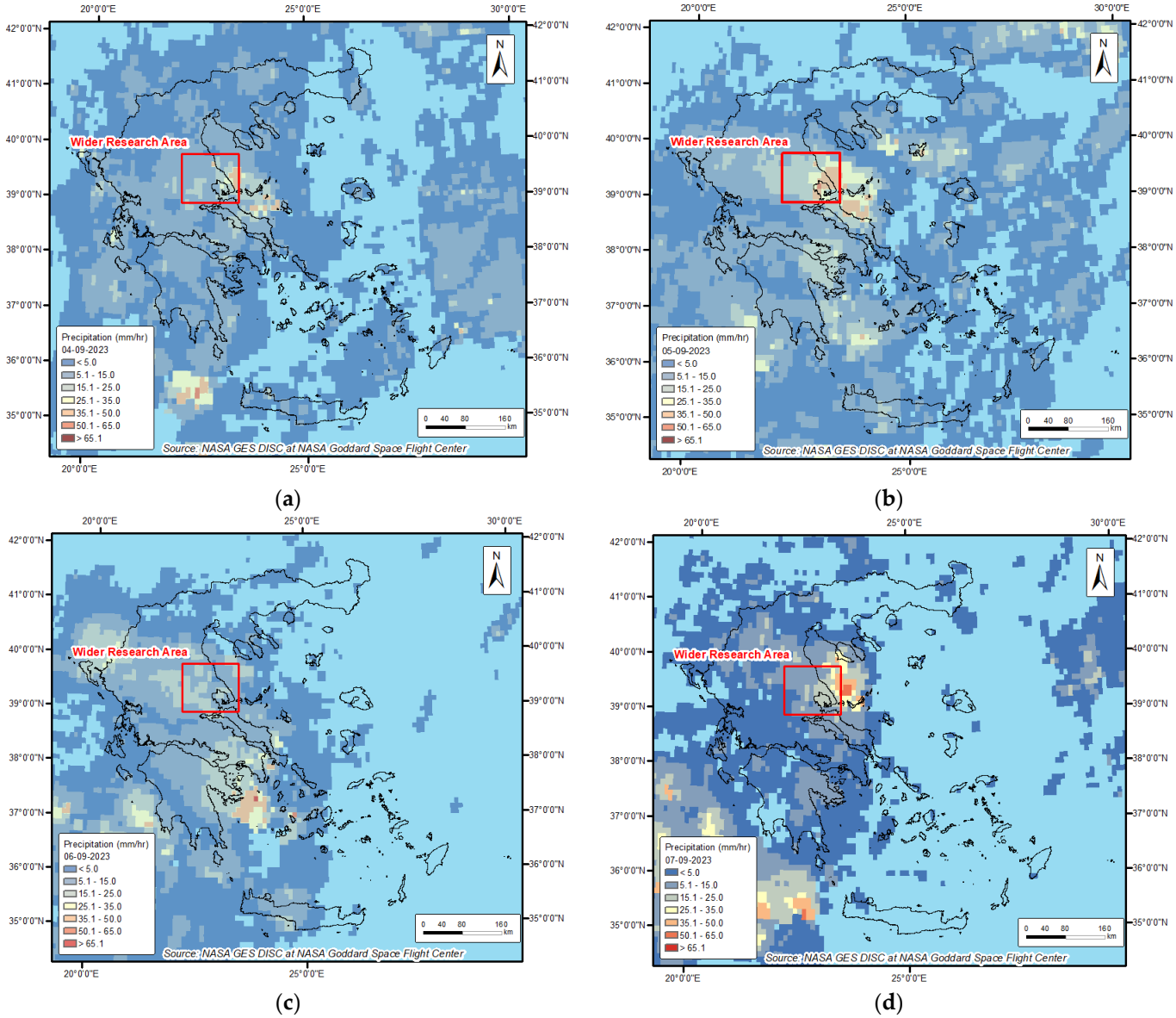

Figure 4. *Cont.*

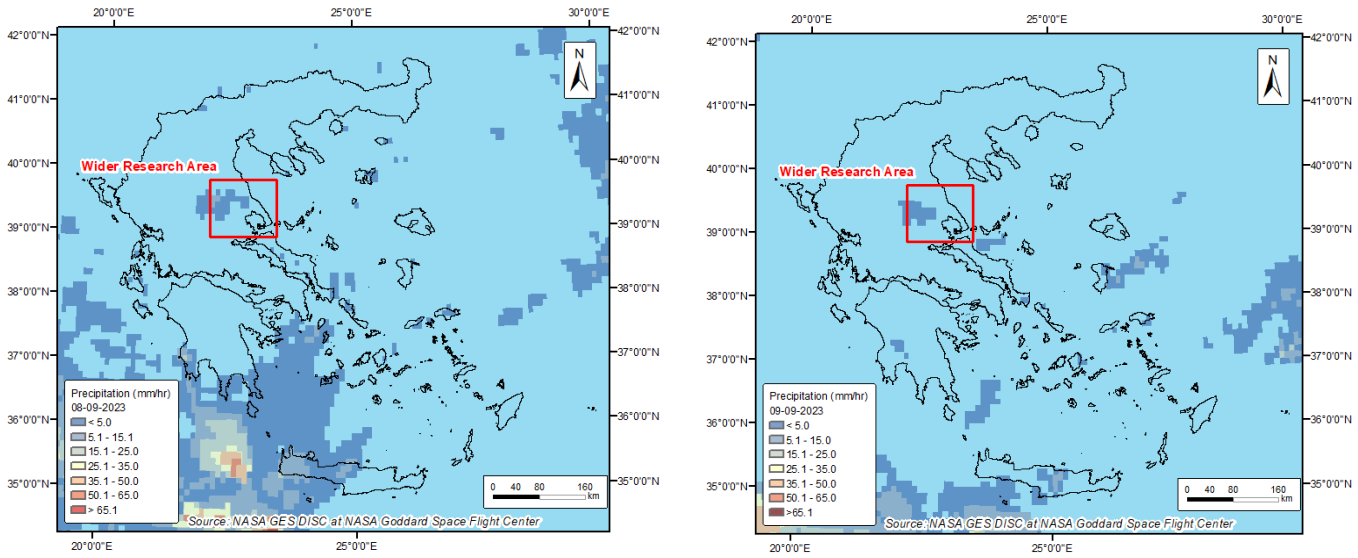

Figure 4. (**a**) Hourly accumulated precipitation 4 September 2023; (**b**) hourly accumulated precipitation 5 September 2023; (**c**) hourly accumulated precipitation 6 September 2023; (**d**) hourly accumulated precipitation 7 September 2023; (**e**) hourly accumulated precipitation 8 September 2023; (**f**) hourly accumulated precipitation 9 September 2023.

As shown in Figure 4a, on the 4th of September, a notable increase in the rainfall amount occurred, peaking at around 10 mm/h. The most intense rainfall happened on 7 September, with the highest peak reaching approximately 35 mm/h, indicating the storm's core activity. Following this, the rainfall intensity decreased, with intermittent showers reaching up to 15 mm/h on 7 September and another peak of about 10–15 mm/h on 8 September. By 9 September, precipitation levels returned to near zero, marking the end of significant rainfall and the storm's impact.

4. Results

The results of the analysis are presented in this section, focusing on the outcomes of the landslide susceptibility mapping, the detection of landslide activity, and the overall validation process of our methodology.

4.1. Landslide Susceptibility Map Produced by the WofE Model

Based on the developed methodology, the WofE model was applied to assess the influence of five conditioning factors on landslide occurrences using GIS overlay analysis (Table 3). For the study area, it was found that surfaces having a slope angle greater than 35° had the higher C value (0.164), indicating a high likelihood of landslide presence. Concerning the aspect conditioning factor, southeast and south facing slopes were found to be more susceptible to landslides, with C values 0.825 and 0.788, respectively. Concave planform curvature, areas that have negative values, were found to have higher C values (0.169), whereas positive profile curvature, upward concave, had the highest C values (0.103). Finally, the SPI values had the highest C value (0.849) in the second class (B), followed by the third class (C) with C value 0.515.

Table 3. Weight of Evidence, contrast values.

Landslide-Related Variables	Classes—Range of Values	W+	W-	Contrast, C
Slope	0°–13°	−0.428	0.053	−0.48
	14°–19°	0.108	−0.047	0.155
	20°–26°	0.003	−0.001	0.005
	27°–34°	0.015	−0.004	0.018
	>35°	0.153	−0.011	0.164
Aspect	North	0.212	−0.027	0.238
	Northeast	0.141	−0.012	0.152
	East	0.398	−0.045	0.443
	Southeast	0.719	−0.107	0.825
	South	0.758	−0.03	0.788
	Southwest	0.15	−0.001	0.151
	West	−0.446	0.005	−0.451
	Northwest	−0.603	0.035	−0.638
Plan Curvature	<−0.2	0.114	−0.054	0.169
	−0.1–0.1	0.018	−0.012	0.029
	>0.2	−0.16	0.06	−0.22
Profile Curvature	<−0.2	−0.014	0.008	−0.021
	−0.1–0.1	−0.061	0.026	−0.087
	>0.2	0.068	−0.035	0.103
Stream Power Index	A: <6209	−0.021	0.358	−0.38
	B: 6210–6609	0.514	−0.001	0.515
	C: 6610–12,818	0.825	−0.023	0.849
	D: 12,819–109,295	−0.128	0.003	−0.131
	E: >109,296	−0.265	0.001	−0.266

By combining the five conditional factors, we generated the landslide susceptibility map illustrated in Figure 5, which was categorized into a five-classification susceptibility scheme: very low (VLS), low (LS), moderate (MS), high (HS), and very high susceptibility (VHS). Examining the spatial distribution of the landslide susceptibility zones, the VHS zone mainly covers steep slopes and ridges, where the topography and other environmental factors create favorable conditions for landslide activity. These high-risk areas tend to be clustered around the central and eastern regions of the map, near settlements such as Makriraxi, Anilio, and Kissos, which highlights the potential threat to nearby communities. The MS and HS zones cover a large portion of the study area, specifically in the mid-slopes of the region. These areas may still experience landslides, but with less frequency. The LS and VLS zones dominate the flatter or less rugged regions of the study area, especially in the western and southern parts of the map, where the terrain is less prone to landslides. The historical landslide events, both data corresponding to the training and testing subsets, are scattered throughout the area, showing a clear overlap with regions of higher susceptibility, particularly in the HS and VHS classes.

As summarized in Table 4, the VLS class, representing 13.18% of the area, accounted for only 3.41% of the landslides, with a relative frequency of 3.95%. The LS class covered 26.33% of the area, with 17.05% of landslides occurring within it, and a relative frequency of 9.90%. The MS class, making up 29.03% of the area, included 19.32% of the landslides, with a relative frequency of 10.17%. The HS class, which covered 22.93% of the area, captured 28.41% of the landslides, showing a relative frequency of 18.94%. Lastly, the VHS class, despite occupying only 8.53% of the total area, contained 31.82% of the landslides, and had the highest relative frequency of 57.04%.

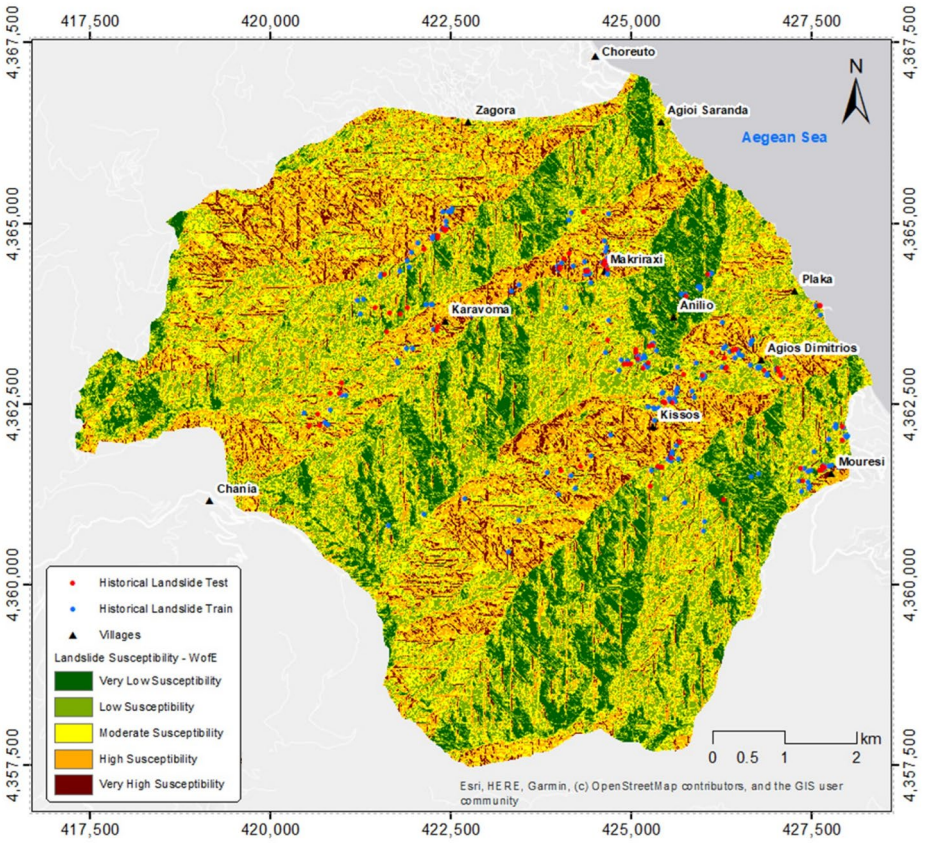

Figure 5. Landslide susceptibility map based on WofE model.

Table 4. Landslide susceptibility classes—relative frequency of landslides test database.

Landslide Susceptibility	Area (%)	Landslide Percentage (%)	Relative Frequency of Landslides (%)
Very Low Susceptibility (VLS)	13.18	3.41	3.95
Low Susceptibility (LS)	26.33	17.05	9.90
Moderate Susceptibility (MS)	29.03	19.32	10.17
High Susceptibility (HS)	22.93	28.41	18.94
Very High Susceptibility (VHS)	8.53	31.82	57.04

These results indicate that landslide occurrences are strongly correlated with areas classified as having high and very high susceptibility, validating the effectiveness of the susceptibility model in predicting potential landslide-prone areas. The significantly higher relative frequency of landslides in the VHS class highlights the accuracy of the classification, as this category is most densely associated with actual landslide events from the test database.

4.2. Landslide Detection Map

In the landslide detection phase of our analysis, we employed the four indices to assess changes in the study area before and after Storm Daniel. Figure 6a–d illustrate the spatial distribution of these indices across the study area, with each index providing unique insights into potential landslide activity. The spatial distribution of NDVI changes reveals significant vegetation loss, particularly along the river network and in areas with steep slopes, where landslide potential is high. The red and orange zones (ranging from −0.55

to −0.15) indicate the most severe decreases in NDVI, suggesting substantial vegetation disturbance or loss. Evidence of landslides was also identified along the road network, where the negative NDVI changes coincide with known landslide occurrences. Quite similar spatial distribution can be observed for the NDMI and BSI change index, with some slight differences at the western regions of the study area. The SAR amplitude changes reflect terrain and surface condition alterations, such as changes in radar reflectance, hillslope geometry, surface roughness, and dielectric properties of the ground, which may be helpful in identifying areas prone to the manifestation of landslides. The areas highlighted in red and orange indicate significant changes in SAR width, which in our case are areas with steep slopes and in proximity to the river network, where soil saturation and runoff are more intense.

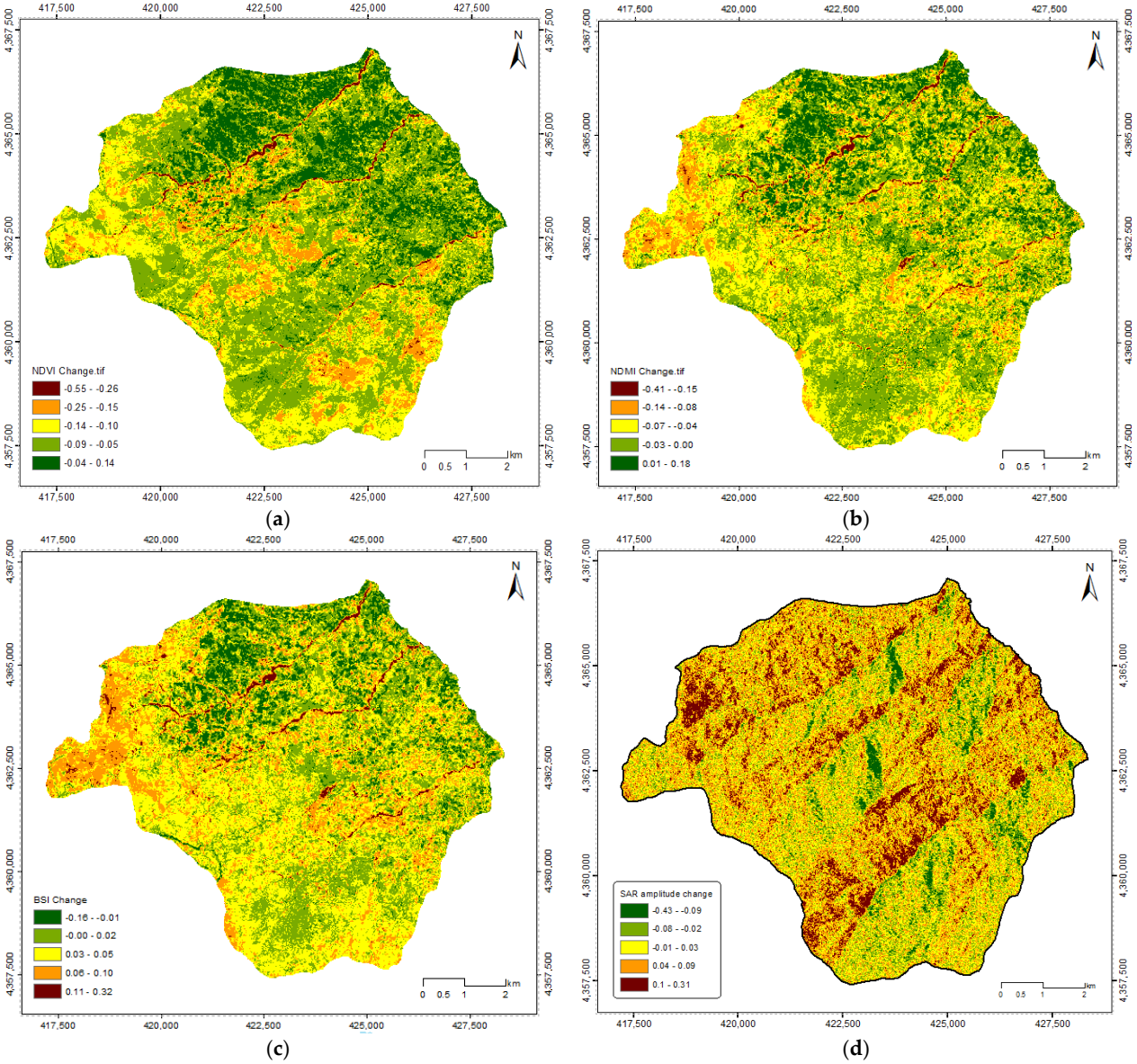

Figure 6. (**a**) Spatial distribution of NDVI change; (**b**) spatial distribution of NDMI change; (**c**) spatial distribution of BSI change; and (**d**) spatial distribution of SAR amplitude change.

By combining the four indices, the Rapid Landslide Detection map has been produced based on a five-level probability scheme utilizing the RLD model (Figure 7a). The pattern highlights the important role of topography and proximity to river networks in determining

landslide susceptibility, with the most severe impacts expected in the steeper, more erosion-prone areas.

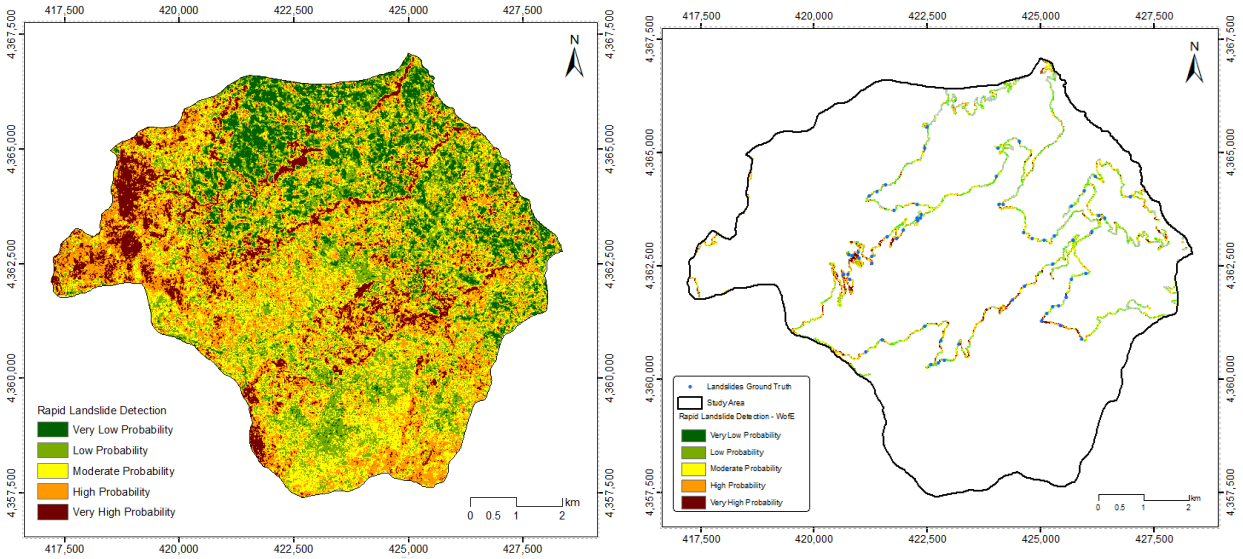

(**a**) (**b**)

Figure 7. (**a**) The Rapid Landslide Detection Potential map; (**b**) Rapid Landslide Detection Potential–WofE map along a 50 m buffer zone road network.

In the landslide detection phase, we analyzed a buffered zone extending 50 m from the road to verify the effectiveness of the developed methodology (Figure 7b). This approach was adopted because our field investigations were conducted along the road extent, making the immediate surroundings particularly relevant for evaluating landslide occurrences. By focusing on this buffer zone, we were able to ensure that the methods were tested in an area closely related to the road network, which is a critical infrastructure subject to landslide risks. This analysis allowed us to assess how well the methodology performs in detecting landslides in proximity to the road, where such events are most likely to cause significant disruption.

4.3. Validation–Ground Truth–Field Surveys

The results of our analysis, as shown in Table 5, categorize the study area into five Landslide Detection Potential classes: Very Low (VLP), Low (LP), Moderate (MP), High (HP), and Very High Potential (VHP). Each class is characterized by its percentage of the total area, the percentage of landslides detected within that area, and the relative frequency of ground truth landslides.

Table 5. Landslide Detection Potential Classes–Relative Frequency of Ground Truth Landslides.

Landslide Detection Potential	Area (%)	Landslide Percentage (%)	Relative Density of Ground Truth Landslides (%)
Very Low Potential (VLP)	21.40	3.33	2.38
Low Potential (LP)	25.21	11.67	7.07
Moderate Potential (MP)	22.18	21.67	14.93
High Potential (HP)	20.21	30.00	22.69
Very High Potential (VHP)	10.99	33.33	46.36

The VHP class, covering 21.40% of the area, contained 3.33% of the detected landslides, with a relative frequency of 2.38%. The LP class, occupying 25.21% of the area, accounted

for 11.67% of the landslides, with a relative frequency of 7.07%. The MP class covered 22.18% of the area and had 21.67% of the landslides, with a relative frequency of 14.93%. The HP class, representing 20.21% of the area, showed a substantial increase, with 30.00% of the landslides and a relative frequency of 22.69%. Finally, the VHP class, which occupied only 10.99% of the area, had the highest concentration of landslides, with 33.33% of the total, and a relative frequency of 46.36%.

These results indicate a clear correlation between higher detection potential classes and the relative density of actual landslides, with landslides being more concentrated in areas classified as having high or very high potential.

Regarding the validation of the improvement achieved by combining the three models, it was found that the AUC value for the RLD-WofE model (0.758) is higher than that of the RLD-Slope model (0.719) and the RLD model (0.696), indicating improved performance in landslide detection when incorporating the WofE methodology (Figure 8). Table 6 shows the AUC values, the standard errors, and the 95% confidence intervals for the three models. Accordingly, during the relative pairwise comparison of the ROC curves between the RLD and RLD-WofE models, it was found that the improvement in detection performance using the RLD-WofE model is statistically significant, since the value of the z-statistic metric is 2.044, with a significance level of $p = 0.041$ (Table 7). A similar statistically significant difference has been observed between the RLD and RLD-Slope model, and the RLD-Slope and RLD-WofE model.

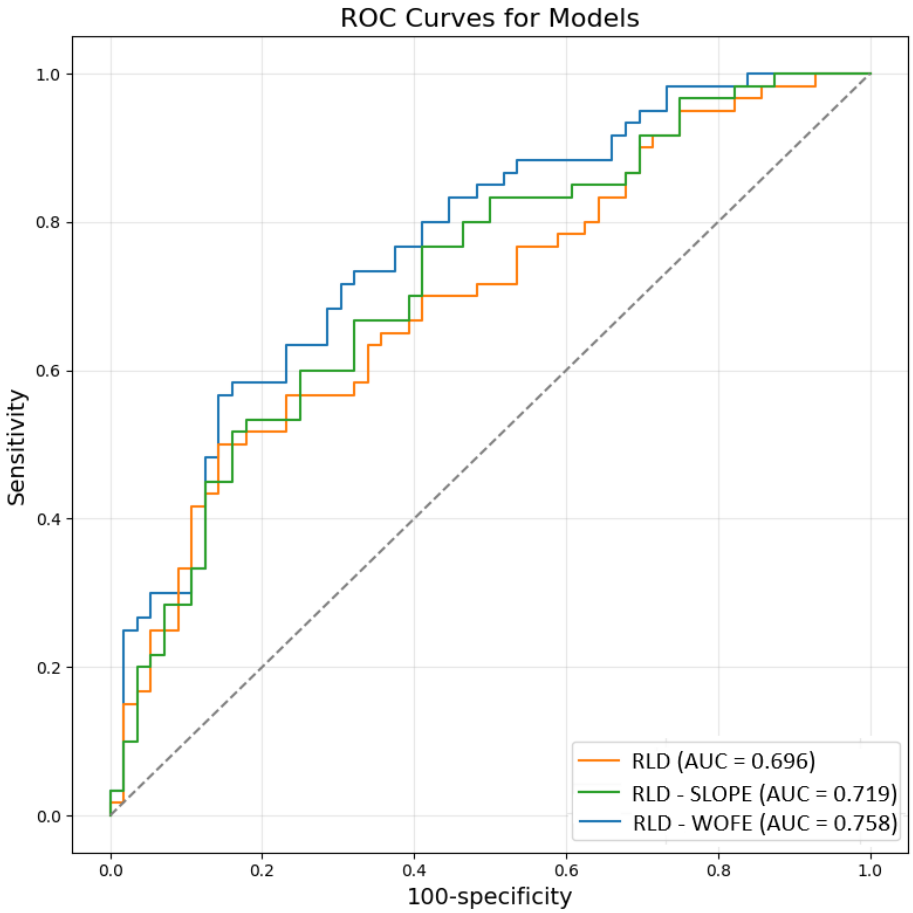

Figure 8. Sensitivity, 100-specificity, and ROC curves for the test dataset of RLD, RLD-Slope, and RLD-WofE models.

Table 6. AUC Metrics of RLD, RLD-Slope, and RLD-WofE models.

Models	AUC Values	Standard Error	95% Confidence Interval
RLD	0.696	0.0479	0.606 to 0.777
RLD-Slope	0.719	0.0421	0.621 to 0.803
RLD-WofE	0.758	0.0441	0.671 to 0.831

Table 7. Pairwise comparison of ROC curves of RLD, RLD-Slope, and RLD-WofE models.

Statistical Metrics	RLD–RLD-WofE	RLD–RLD-Slope	RLD-Slope–RLD-WofE
Difference Between Areas	0.0614	0.0233	0.0620
Standard Error	0.0300	0.0167	0.0283
95% Confidence Interval	0.00253 to 0.120	0.00280 to 0.0722	−0.0065 to 0.1175
z Statistic	2.044	2.118	2.191
Significance Level	$p = 0.041$	$p = 0.034$	$p = 0.029$

Furthermore, it was found (Table 8) that the RLD-WofE model achieves the highest precision (0.680), followed by the RLD-Slope model (0.651) and the RLD model (0.642), indicating a reduced number of false positives, which enhances the reliability of the predictions. Regarding the recall, the RLD-WofE model achieves higher values (0.760) compared to that achieved by the RLD-Slope model (0.696) and the RLD model (0.664). The F1 score, which balances precision and recall, is also higher for the RLD-WofE model (0.717), confirming the overall better performance in identifying landslide-prone areas, maintaining fewer false positives and ensuring comprehensive detection.

Table 8. Statistical metrics.

Models	Precision	Recall	F1-Score
RLD	0.642	0.664	0.653
RLD-Slope	0.651	0.696	0.673
RLD-WofE	0.680	0.760	0.717

The following figures (Figures 9 and 10) illustrate the results of our field investigation, where we identified landslide occurrences along the road network within the study area. The central map highlights the locations of observed landslides, represented by red marks, corresponding to actual sites examined during the field trip. Each of the images surrounding the map provides visual documentation of the landslides at specific locations, further validating the accuracy of our remote sensing and landslide detection methods. These photos offer a clear representation of the various types of landslide activity, including slope failures and erosion near infrastructure, confirming the effectiveness of the applied detection models and reinforcing the importance of monitoring these high-risk zones.

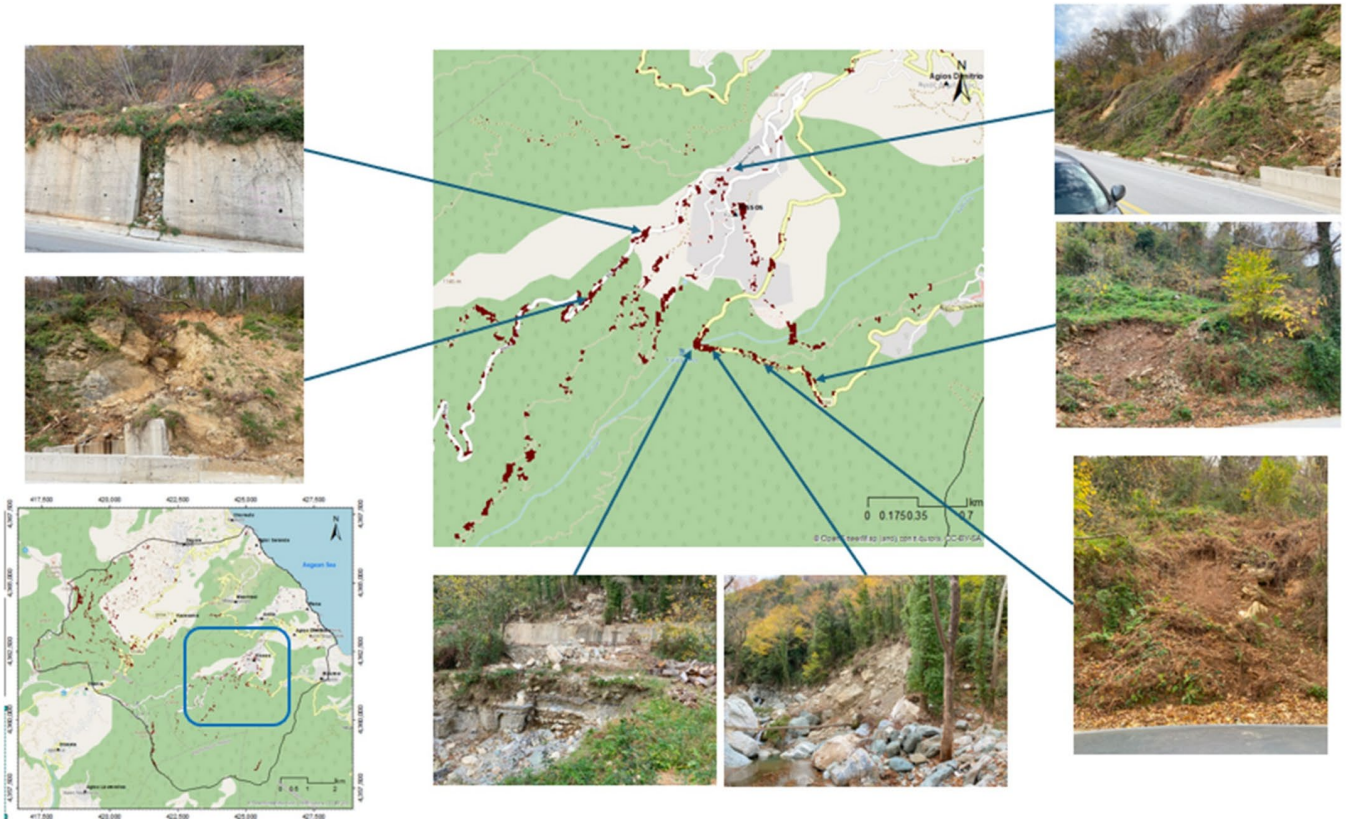

Figure 9. Field surveys—ground truth evidence—high and very high susceptibility zones.

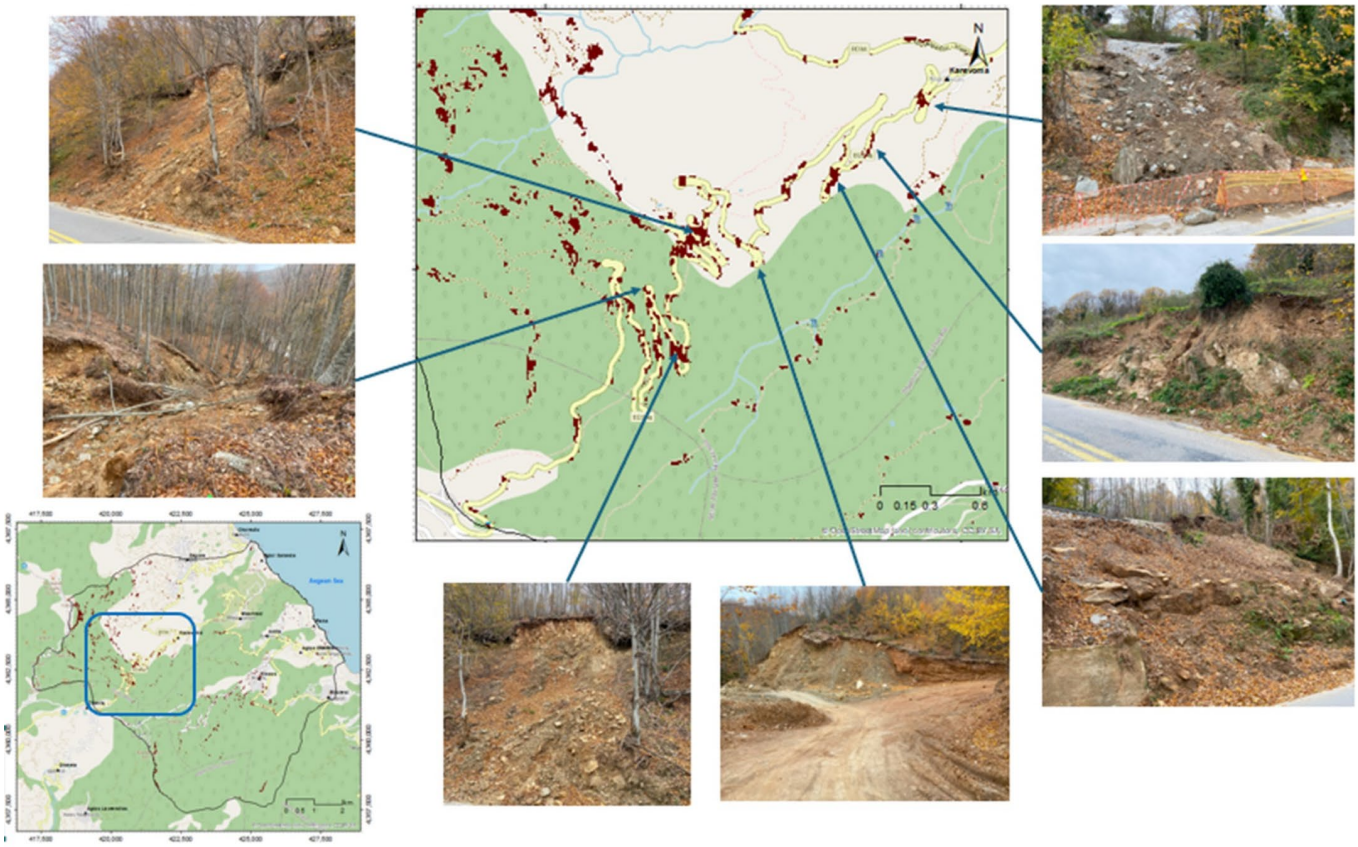

Figure 10. Field surveys—ground truth evidence—high and very high susceptibility zones.

5. Discussion

As mentioned by Ray et al. [95], traditional methods for studying the manifestation and the evolution of landslides, such as analyzing aerial photographs and conducting extensive field surveys, are time-consuming and costly. On the other hand, timely and accurate information about landslide occurrences and their evolution is critical not only during the emergency phase, allowing for better crisis management by decision-makers, but also in the recovery phase. To address these challenges and provide faster, more accurate insights into landslide dynamics, new technologies have emerged that offer more efficient methods of data collection and analysis. Advanced remote sensing technologies, which may offer high spatial and temporal resolution, make landslide studies more efficient and scalable. A recent study by Peters et al. [39] emphasizes the significant potential of using advanced remote sensing and machine learning techniques to enhance landslide detection, suggesting further improvements through finer spatial resolution data, more precise landslide inventory boundaries, and additional data layers such as soil moisture and geological structure.

Our study introduces a cloud-based application of satellite-based remote sensing, implemented in the GEE platform using optical and SAR imagery. The success of implementing the GEE platform in landslide detection lies in its robust computational power hosted in the cloud, allowing for the efficient processing of large-scale geospatial datasets [41]. Similarly, Singh et al. [96] report that the ability to handle large datasets and perform complex computations quickly made the GEE platform an ideal tool for conducting rapid, accurate assessments of landslide susceptibility and detection following extreme natural phenomena. Our methodology goes beyond simple remote sensing analysis by integrating these indices with the outcomes of a WofE model. The WofE model, a widely utilized approach for analyzing landslide susceptibility, allowed us to incorporate geomorphological variables, such as slope, aspect, plan and profile curvature, and stream power index, to identify regions that are characterized by high and very high susceptibility values. By combining these susceptibility maps with changes in NDVI, NDMI, BSI, and SAR amplitude ratio, we were able to mask out areas of low susceptibility, focusing our analysis on regions more likely to experience landslides.

Concerning the use of the optical satellite indices, NDVI, NDMI, and BSI enhanced this analysis by offering additional layers of information on vegetation health, soil moisture, and exposed soil areas, respectively. NDVI was found to be a significant parameter for monitoring vegetation density, which can serve as an indicator of underlying slope surface instability. NDMI provides insights into moisture content in vegetation and the upper soil layer, a crucial factor in assessing landslide risk post-rainfall. From a hydrogeological perspective, both groundwater and surface water infiltrate the loose materials of the soil mantle, weathering zone, and colluvium. This infiltration increases the pore pressure and decreases the shear strength of these geological formations, leading to their failure.

In our study, the BSI successfully identified areas where vegetation had been stripped away, exposing potentially unstable bare soil surfaces. However, as reported by Ariza et al. [18], the BSI can serve as a complementary method to support traditional interferometric SAR analysis. By incorporating additional remote sensing indices, such as NDVI or SAVI (Soil-Adjusted Vegetation Index), using pre- and post-event imagery, the effects of vegetation change can be mitigated. This approach leads to improved BSI values more accurately linked to landslide-prone areas.

In reference to the SAR imagery, our outcomes align with Mondini et al. [15], who report that SAR amplitude changes, as seen in pre- and post-event Sentinel-1 images, can effectively detect landslides in various terrains and conditions. In most cases, the observed decrease in SAR amplitude was attributed to landslide scars and damage, which reduce

backscattering reflectance relative to the pre-failure ground surface [44]. However, we also identified numerous instances where SAR amplitude changes were not related to landslides. Often, these changes occurred in farmlands, where regular ground surface alterations and significant variations in water content due to flooding can affect SAR reflectivity [35,36,44]. This highlights the importance of careful interpretation of SAR data to distinguish between true landslide events and other surface changes.

The results of the WofE landslide susceptibility map offer detailed insights into how various terrain and hydrological factors influence landslide occurrence, with notable patterns emerging across different variables. As expected, steeper slopes show a higher susceptibility to landslides, with slopes greater than 35° having the highest positive contrast (C = 0.164). This confirms that steeper gradients are more prone to landslides due to increased gravitational stress. In contrast, gentler slopes (0°–13°) exhibit negative contrast values (C = −0.480), indicating low landslide susceptibility in flatter areas. Southern-facing slopes, especially those facing southeast (C = 0.825) and south (C = 0.788), exhibit significantly higher susceptibility, likely due to increased solar radiation that accelerates weathering and drying, making the soil more unstable. In contrast, northwest-facing slopes (C = −0.638) show the least susceptibility, perhaps due to lower solar radiation and reduced weathering effects.

Plan curvature results indicate that concave surfaces (<−0.2) have a positive correlation with landslides (C = 0.169), suggesting that these areas accumulate water, contributing to increased erosion and instability. Conversely, profile curvature shows that convex areas (>0.2) are slightly more susceptible (C = 0.103), potentially due to surface runoff accumulation that weakens the slope material.

Areas with moderate to high SPI values (6.610–12.818) show the strongest positive correlation (C = 0.849), indicating that regions with significant water flow and erosion energy are more prone to landslides. Extremely high SPI values (>109.296), however, exhibit negative contrast (C = −0.266), suggesting that while erosion is important, too much flow energy might not correlate directly with landslide occurrences, possibly due to changes in terrain characteristics.

Overall, the developed methodology demonstrated satisfactory detection capability, as 69% of the relative density of landslides recorded during an extensive field survey along the main road network in the research area were correctly identified within regions characterized by high to very high potential. The ROC curve analysis further confirmed the detection capability when compared to the performance of the other models. The RLD-WofE model achieved an AUC value of 0.758, outperforming the RLD model, which had an AUC value of 0.696, and the RLD-Slope model, which reached a value of 0.719. The pairwise comparison of the ROC curves revealed a statistically significant difference between all models, confirming the improved performance of the RLD-WofE model in accurately detecting landslide-prone areas. Furthermore, considering the performance of the proposed model in reducing false positives, the RLD-WofE model was better, as evidenced by its higher precision (0.680) compared to the RLD-Slope model (0.651) and the RLD model (0.642). The significant increase in recall, as reflected in the higher value (0.760, highlights the better performance of the RLD-WofE model in detecting real landslides overall. Correspondingly, the higher F1 score (0.717) further confirms the balanced performance of the RLD-WofE model.

Regarding the use of the WofE model for landslide susceptibility assessment, its effectiveness was demonstrated in reducing false positive cases identified in the first phase of the developed methodology. While Machine Learning methods, including deep learning, have shown high accuracy in landslide susceptibility assessment and, in some cases, landslide detection using high-resolution satellite imagery, their application often demands extensive

preparation. A critical requirement for these models is the creation of balanced datasets comprising both landslide and non-landslide cases, which can be challenging in regions with limited data availability or uniform geological and environmental characteristics. In contrast, the WofE model employed in this study does not rely on non-landslide data, making it particularly well-suited for areas such as our study region, where all observed landslide events occurred within a single geological formation, and historical landslide data were readily available. This practical and adaptable approach allows for rapid implementation, ensuring effectiveness in time-sensitive scenarios, such as those following extreme rainfall events.

However, certain limitations must be acknowledged. First, the accuracy of the landslide detection is dependent on the spatial and temporal resolution of the satellite data, which may miss smaller or rapidly evolving landslides. Notti et al. [41] report that in their GEE-based landslide detection model, the success rate of detection drops 20% regarding small landslides (less than 100 m^2). Additionally, the effectiveness of the indices used, such as NDVI and NDMI, can be influenced by vegetation regrowth, which may obscure signs of landslides in post-event imagery. Another serious drawback is the difference that may be crucial in the land use cover. In our case, the methodology works well in areas of forest and less accurate in cultivated areas. Furthermore, the integration of the Weight of Evidence model relies on historical landslide data, which may not always be available or sufficiently detailed for certain regions, potentially limiting the transferability of the methodology to areas with less robust historical data. Finally, while the use of SAR and optical data provided robust results, atmospheric interference and dense cloud cover can occasionally limit the quality of optical imagery [61].

Despite these limitations, the methodology presents a valuable tool for rapid, large-scale landslide detection, especially in regions where field surveys are impractical or infeasible. Future work could focus on addressing the limitations encountered in this study and further refining the methodology. One potential improvement lies in incorporating higher-resolution satellite imagery to enhance the detection of smaller and more localized landslides, which are often missed in lower-resolution data. Additionally, integrating machine learning techniques, such as deep learning models, could help automate the classification process, improve the detection accuracy, and reduce reliance on manually defined thresholds for indices like NDVI, NDMI, and BSI. In particular, in areas with adequate data availability, the integration of deep learning models could be explored to automate the classification process and improve detection accuracy. In areas where the formation of a balanced database is feasible in combination with the utilization of high-resolution datasets for landslide detection, the application of deep learning techniques may exceed the performance of traditional methods. Finally, expanding the methodology to other regions with varying climates, geological conditions, and topography could enhance its adaptability and generalizability. This would allow for the validation of the approach across different environments and ensure its effectiveness on a global scale.

6. Conclusions

The current study successfully demonstrates the potential of integrating satellite-based optical and SAR data, processed through the GEE platform, for the rapid detection of landslides caused by extreme rainfall events. By utilizing NDVI, NDMI, BSI, and SAR amplitude ratio, we were able to efficiently assess vegetation health, soil moisture, and exposed soil conditions before and after the event. The combined analysis of SAR amplitude, NDVI, NDMI, and BSI index effectively identified potential landslide zones in the study area following an extreme rainfall event. The steepest slopes, particularly those exhibiting significant SAR amplitude changes and a notable increase in the BSI, suggest terrain

disturbances indicative of landslides. Further validation was provided by the observed decrease in vegetation (NDVI) and potential moisture loss (NDMI) in these regions. The integration of these indices with the WofE model, based on morphological parameters such as slope, aspect, and curvature, provided a robust framework for identifying areas with high and very high landslide susceptibility. Our methodology, applied to the real-world scenario of Storm Daniel in central Greece, yielded significant insights into landslide-prone regions. The detection of landslide events with a relative density of 69% within regions characterized as having high to very high susceptibility underscores the practical applicability of the approach. Furthermore, the use of pre- and post-event imagery, coupled with the WofE model, allowed for an accurate focus on regions where landslides were most likely to occur, minimizing false positives and improving detection accuracy. Despite the limitations of the developed methodology, which include the ability to detect small landslides (less than 100 m^2) and the dependence on the availability of historical data related to landslide phenomena in the study area, the methodology demonstrates significant potential for rapid, large-scale landslide detection. Possible future improvements of the methodology, such as the integration of higher resolution satellite images as well as the use of advanced machine learning techniques, could improve the detection accuracy. The possibility of extending the approach to different study areas where different geoenvironmental and climatic conditions prevail will also be important and will further validate the adaptability and global applicability of the developed methodology. The successful application of this methodology during Storm Daniel highlights its potential to significantly improve disaster management strategies in regions vulnerable to extreme weather events, offering a practical solution for timely response and mitigation efforts.

Author Contributions: Conceptualization, P.T., and A.-A.C.; methodology, P.T., W.C. and A.-A.C.; investigation, A.-A.C., P.T. and I.I.; writing—original draft preparation, A.-A.C. and P.T.; writing—review and editing, P.T., I.I. and W.C.; supervision, P.T. All authors have read and agreed to the published version of the manuscript.

Funding: This research received no external funding.

Data Availability Statement: The data presented in this study are available on request from the corresponding author.

Conflicts of Interest: The authors declare no conflicts of interest.

References

1. Reichenbach, P.; Rossi, M.; Malamud, B.D.; Mihir, M.; Guzzetti, F. A review of statistically-based landslide susceptibility models. *Earth Sci. Rev.* **2018**, *180*, 60–91. [CrossRef]
2. He, Q.; Shahabi, H.; Shirzadi, A.; Li, S.; Chen, W.; Wang, N.; Chai, H.; Bian, H.; Ma, J.; Chen, Y.; et al. Landslide spatial modelling using novel bivariate statistical based Naïve Bayes, RBF Classifier, and RBF Network machine learning algorithms. *Sci. Total Environ.* **2019**, *663*, 1–15. [CrossRef] [PubMed]
3. Donnini, M.; Santangelo, M.; Gariano, S.L.; Bucci, F.; Peruccacci, S.; Alvioli, M.; Althuwaynee, O.; Ardizzone, F.; Bianchi, C.; Bornaetxea, T.; et al. Landslides Triggered by an Extraordinary Rainfall Event in Central Italy on September 15, 2022. *Landslides* **2023**, *20*, 2199–2211. [CrossRef]
4. Dolojan, N.L.J.; Moriguchi, S.; Hashimoto, M.; Tinh, N.X.; Tanaka, H.; Terada, K. Hydrologic-Geotechnical Modelling of Shallow Landslide and Flood Hazards Caused by Heavy Rainfall. *Eng. Geol.* **2023**, *323*, 107184. [CrossRef]
5. Smith, H.G.; Neverman, A.J.; Betts, H.; Spiekermann, R. The Influence of Spatial Patterns in Rainfall on Shallow Landslides. *Geomorphology* **2023**, *437*, 108795. [CrossRef]
6. Ghorbanzadeh, O.; Didehban, K.; Rasouli, H.; Kamran, K.V.; Feizizadeh, B.; Blaschke, T. An application of sentinel-1, sentinel-2, and GNSS data for landslide susceptibility mapping. *ISPRS Int. J. Geo-Inf.* **2020**, *9*, 561. [CrossRef]
7. Handwerger, A.L.; Huang, M.-H.; Jones, S.Y.; Amatya, P.; Kerner, H.R.; Kirschbaum, D.B. Generating landslide density heatmaps for rapid detection using open-access satellite radar data in Google Earth Engine. *Nat. Hazards Earth Syst. Sci.* **2022**, *22*, 753–773. [CrossRef]

8. Wasowski, J.; Bovenga, F. Remote sensing of landslide motion with emphasis on satellite multi-temporal interferometry applications: An overview. In *Landslide Hazards Risks Disasters*, 2nd ed.; Elsevier: Amsterdam, The Netherlands, 2022; pp. 365–438.
9. Wu, W.; Zhang, Q.; Singh, V.P.; Wang, G.; Zhao, J.; Shen, Z.; Sun, S. A Data-Driven Model on Google Earth Engine for Landslide Susceptibility Assessment in the Hengduan Mountains, the Qinghai–Tibetan Plateau. *Remote Sens.* **2022**, *14*, 4662. [CrossRef]
10. Cruden, D.M.; Varnes, D.J. Landslide Types and Processes. In *Landslides: Investigation and Mitigation*; Turner, A.K., Schuster, R.L., Eds.; Transportation Research Board, US National Research Council: Washington, DC, USA, 1996.
11. Zhao, C.; Lu, Z. Remote Sensing of Landslides—A Review. *Remote Sens.* **2018**, *10*, 279. [CrossRef]
12. Peng, J.; Wang, S.; Wang, Q.; Zhuang, J.; Huang, W.; Zhu, X.; Leng, Y.; Ma, P. Distribution and genetic types of loess landslides in China. *J. Asian Earth Sci.* **2019**, *170*, 329–350. [CrossRef]
13. Guzzetti, F.; Carrara, A.; Cardinali, M.; Reichenbach, P. Landslide hazard evaluation: A review of current techniques and their application in a multi-scale study, Central Italy. *Geomorphology* **1999**, *31*, 181–216. [CrossRef]
14. Fiorucci, F.; Giordan, D.; Santangelo, M.; Dutto, F.; Rossi, M.; Guzzetti, F. Criteria for the optimal selection of remote sensing optical images to map event landslides. *Nat. Hazards Earth Syst. Sci.* **2018**, *18*, 405–417. [CrossRef]
15. Mondini, A.C.; Santangelo, M.; Rocchetti, M.; Rossetto, E.; Manconi, A.; Monserrat, O. Sentinel-1 SAR Amplitude Imagery for Rapid Landslide Detection. *Remote Sens.* **2019**, *11*, 760. [CrossRef]
16. Casagli, N.; Intrieri, E.; Tofani, V.; Gigli, G.; Raspini, F. Landslide detection, monitoring and prediction with remote-sensing techniques. *Nat. Rev. Earth Environ.* **2023**, *4*, 51–64. [CrossRef]
17. Casagli, N.; Cigna, F.; Bianchini, S.; Hölbling, D.; Füreder, P.; Righini, G.; Conte, S.D.; Friedl, B.; Schneiderbauer, S.; Iasio, C.; et al. Landslide mapping and monitoring by using radar and optical remote sensing: Examples from the EC-FP7 project SAFER. *Remote Sens. Appl. Soc. Environ.* **2016**, *4*, 92–108. [CrossRef]
18. Ariza, A.; Davila, N.A.; Kemper, H.; Kemper, G. Landslide Detection in Central America Using the Differential Bare Soil Index. *Int. Arch. Photogramm. Remote Sens. Spat. Inf. Sci.* **2021**, *XLIII-B3-2021*, 471–478. [CrossRef]
19. Shahabi, H.; Rahimzad, M.; Tavakkoli Piralilou, S.; Ghorbanzadeh, O.; Homayouni, S.; Blaschke, T.; Lim, S.; Ghamisi, P. Unsupervised deep learning for landslide detection from multispectral sentinel-2 imagery. *Remote Sens.* **2021**, *13*, 4698. [CrossRef]
20. Phakdimek, S.; Komori, D.; Chaithong, T. Combination of Optical Images and SAR Images for Detecting Landslide Scars, Using a Classification and Regression Tree. *Int. J. Remote Sens.* **2023**, *44*, 3572–3606. [CrossRef]
21. Hervás, J.; Barredo, J.I.; Rosin, P.L.; Pasuto, A.; Mantovani, F.; Silvano, S. Monitoring landslides from optical remotely sensed imagery: The case history of Tessina landslide, Italy. *Geomorphology* **2003**, *54*, 63–75. [CrossRef]
22. Qin, Y.; Lu, P.; Li, Z. Landslide inventory mapping from bitemporal 10 m sentinel-2 images using change detection based markov random field. *Int. Arch. Photogramm. Remote Sens. Spat. Inf. Sci.* **2018**, *42*, 1447–1452. [CrossRef]
23. Fayne, J.V.; Ahamed, A.; Roberts-Pierel, J.; Rumsey, A.C.; Kirschbaum, D. Automated Satellite-Based Landslide Identification Product for Nepal. *Earth Interact.* **2019**, *23*, 1–21. [CrossRef]
24. Piralilou, S.T.; Shahabi, H.; Pazur, R. Automatic Landslide Detection Using Bi-Temporal Sentinel 2 Imagery. *GI_Forum* **2021**, *9*, 39–45. [CrossRef]
25. Colesanti, C.; Wasowski, J. Investigating landslides with space-borne Synthetic Aperture Radar (SAR) interferometry. *Eng. Geol.* **2006**, *88*, 173–199. [CrossRef]
26. Hilley, G.E.; Bürgmann, R.; Ferretti, A.; Novali, F.; Rocca, F. Dynamics of slow-moving landslides from permanent scatterer analysis. *Science* **2004**, *304*, 1952–1955. [CrossRef] [PubMed]
27. Roering, J.J.; Stimely, L.L.; Mackey, B.H.; Schmidt, D.A. Using DInSAR, airborne LiDAR, and archival air photos to quantify landsliding and sediment transport. *Geophys. Res. Lett.* **2009**, *36*, L19402. [CrossRef]
28. Handwerger, A.L.; Huang, M.-H.; Fielding, E.J.; Booth, A.M.; Bürgmann, R. A shift from drought to extreme rainfall drives a stable landslide to catastrophic failure. *Sci. Rep.* **2019**, *9*, 1569. [CrossRef]
29. Huang, H.; Chen, Y.; Clinton, N.; Wang, J.; Wang, X.; Liu, C.; Gong, P.; Yang, J.; Bai, Y.; Zheng, Y.; et al. Mapping major land cover dynamics in Beijing using all Landsat images in Google Earth Engine. *Remote Sens. Environ.* **2017**, *202*, 166–176. [CrossRef]
30. Intrieri, E.; Raspini, F.; Fumagalli, A.; Lu, P.; Del Conte, S.; Farina, P.; Allievi, J.; Ferretti, A.; Casagli, N. The Maoxian landslide as seen from space: Detecting precursors of failure with Sentinel-1 data. *Landslides* **2017**, *15*, 123–133. [CrossRef]
31. Schlögel, R.; Doubre, C.; Malet, J.-P.; Masson, F. Landslide deformation monitoring with ALOS/PALSAR imagery: A D-InSAR geomorphological interpretation method. *Geomorphology* **2015**, *231*, 314–330. [CrossRef]
32. Burrows, K.; Walters, R.J.; Milledge, D.; Densmore, A.L. A systematic exploration of satellite radar coherence methods for rapid landslide detection. *Nat. Hazards Earth Syst. Sci.* **2020**, *20*, 3197–3214. [CrossRef]
33. DeVries, B.; Huang, C.; Armston, J.; Huang, W.; Jones, J.W.; Lang, M.W. Rapid and robust monitoring of flood events using Sentinel-1 and Landsat data on the Google Earth Engine. *Remote Sens. Environ.* **2020**, *240*, 111664. [CrossRef]
34. Jung, J.; Yun, S.-H. Evaluation of Coherent and Incoherent Landslide Detection Methods Based on Synthetic Aperture Radar for Rapid Response: A Case Study for the 2018 Hokkaido Landslides. *Remote Sens.* **2020**, *12*, 265. [CrossRef]

35. Mondini, A.C.; Guzzetti, F.; Chang, K.T.; Monserrat, O.; Martha, T.R.; Manconi, A. Landslide Failures Detection and Mapping Using Synthetic Aperture Radar: Past, Present and Future. *Earth-Sci. Rev.* **2021**, *216*, 103574. [CrossRef]
36. Rignot, E.J.; Van Zyl, J.J. Change detection techniques for ERS-1 SAR data. *IEEE Trans. Geosci. Remote* **1993**, *31*, 896–906. [CrossRef]
37. Scheip, C.M.; Wegmann, K.W. HazMapper: A global open-source natural hazard mapping application in Google Earth Engine. *Nat. Hazards Earth Syst. Sci.* **2021**, *21*, 1495–1511. [CrossRef]
38. Notti, D.; Cignetti, M.; Godone, D.; Giordan, D. Semi-Automatic Mapping of Shallow Landslides Using Free Sentinel-2 and Google Earth Engine. *Nat. Hazards Earth Syst. Sci. Discuss.* **2023**, *23*, 2625–2648. [CrossRef]
39. Peters, S.; Liu, J.; Keppel, G.; Wendleder, A.; Xu, P. Detecting Coseismic Landslides in GEE Using Machine Learning Algorithms on Combined Optical and Radar Imagery. *Remote Sens.* **2024**, *16*, 1722. [CrossRef]
40. Adriano, B.; Yokoya, N.; Miura, H.; Matsuoka, M.; Koshimura, S. A Semiautomatic Pixel-Object Method for Detecting Land-slides Using Multitemporal ALOS-2 Intensity Images. *Remote Sens.* **2020**, *12*, 561. [CrossRef]
41. Gorelick, N.; Hancher, M.; Dixon, M.; Ilyushchenko, S.; Thau, D.; Moore, R. Google Earth Engine: Planetary-Scale Geospatial Analysis for Everyone. *Remote Sens. Environ.* **2017**, *202*, 18–27. [CrossRef]
42. Chowdhury, M.S.; Rahman, M.N.; Sheikh, M.S.; Sayeid, M.A.; Mahmud, K.H.; Hafsa, B. GIS-Based Landslide Susceptibility Mapping Using Logistic Regression, Random Forest, and Decision and Regression Tree Models in Chattogram District, Bangladesh. *Heliyon* **2024**, *10*, e23424. [CrossRef]
43. Shahabi, H.; Hashim, M. Landslide susceptibility mapping using GIS-based statistical models and Remote sensing data in tropical environment. *Sci. Rep.* **2015**, *5*, 9899. [CrossRef] [PubMed]
44. Le Toan, T.; Beaudoin, A.; Riom, J.; Guyon, D. Relating Forest Biomass to SAR Data. *IEEE Trans. Geosci. Remote Sens.* **1992**, *30*, 403–411. [CrossRef]
45. Ghosh, S.; Kumar, D.; Kumari, R. Cloud-Based Large-Scale Data Retrieval, Mapping, and Analysis for Land Monitoring Applications with Google Earth Engine (GEE). *Environ. Chall.* **2022**, *9*, 100605. [CrossRef]
46. Lee, J.S.; Wen, J.H.; Ainsworth, T.L.; Chen, K.S.; Chen, A.J. Improved Sigma Filter for Speckle Filtering of SAR Imagery. *IEEE Trans. Geosci. Remote Sens.* **2008**, *47*, 202–213. [CrossRef]
47. Huang, S.; Tang, L.; Hupy, J.P.; Wang, Y.; Shao, G. A commentary review on the use of normalized difference vegetation index (NDVI) in the era of popular remote sensing. *J. For. Res.* **2021**, *32*, 1–6. [CrossRef]
48. Niraj, K.C.; Singh, A.; Shukla, D.P. Effect of the Normalized Difference Vegetation Index (NDVI) on GIS-Enabled Bivariate and Multivariate Statistical Models for Landslide Susceptibility Mapping. *J. Indian. Soc. Remote Sens.* **2023**, *51*, 1739–1756. [CrossRef]
49. Yang, W.; Wang, Y.; Sun, S.; Wang, Y.; Ma, C. Using Sentinel-2 time series to detect slope movement before the Jinsha River landslide. *Landslides* **2019**, *16*, 1313–1324. [CrossRef]
50. Chaabane, F.Z.; Lamine, S.; Guettouche, M.S.; Bachari, N.E.I.; Hallal, N. Landslide Risk Assessments through Multicriteria Analysis. *ISPRS Int. J. Geo-Inf.* **2024**, *13*, 303. [CrossRef]
51. Gao, B.C. NDWI—A normalized difference water index for remote sensing of vegetation liquid water from space. *Remote Sens. Environ.* **1996**, *58*, 257–266.
52. Huang, F.; Teng, Z.; Guo, Z.; Catani, F.; Huang, J. Uncertainties of Landslide Susceptibility Prediction: Influences of Different Spatial Resolutions, Machine Learning Models and Proportions of Training and Testing Dataset. *Rock Mech. Bull.* **2023**, *2*, 100028. [CrossRef]
53. Roy, P.S.; Sharma, K.P.; Jain, A. Stratification of Density in Dry Deciduous Forest Using Satellite Remote Sensing Digital Data—An Approach Based on Spectral Indices. *J. Biosci.* **1996**, *21*, 723–734. [CrossRef]
54. Lu, M.; Tay, L.T.; Mohamad-Saleh, J. Landslide Susceptibility Analysis Using Random Forest Model with SMOTE-ENN Resampling Algorithm. *Geomat. Nat. Hazards Risk* **2024**, *15*, 2314565. [CrossRef]
55. Xu, K.; Zhao, Z.; Chen, W.; Ma, J.; Liu, F.; Zhang, Y.; Ren, Z. Comparative Study on Landslide Susceptibility Mapping Based on Different Ratios of Training Samples and Testing Samples by Using RF and FR-RF Models. *Nat. Hazards Res.* **2024**, *4*, 62–74. [CrossRef]
56. Peng, Z.; Liu-Zeng, J.; Deng, Y.; Toda, S. Strong earthquake increases seismic hazard in Qinghai, China. Temblor, 13 January 2022. Available online: https://temblor.net/earthquake-insights/strong-earthquake-increases-seismic-hazard-in-qinghai-china-13637/ (accessed on 23 December 2024). [CrossRef]
57. Youssef, A.M.; Pourghasemi, H.R.; Pourtaghi, Z.; Al-Katheeri, M.M. Landslide Susceptibility Mapping Using Random Forest, Boosted Regression Tree, Classification and Regression Tree, and General Linear Models and Comparison of Their Performance at Wadi Tayyah Basin, Asir Region, Saudi Arabia. *Landslides* **2016**, *13*, 839–856. [CrossRef]
58. Liao, M.; Wen, H.; Yang, L. Identifying the Essential Conditioning Factors of Landslide Susceptibility Models Under Different Grid Resolutions Using Hybrid Machine Learning: A Case of Wushan and Wuxi Counties, China. *CATENA* **2022**, *217*, 106428. [CrossRef]
59. Kavzoglu, T.; Sahin, E.K.; Colkesen, I. Selecting Optimal Conditioning Factors in Shallow Translational Landslide Susceptibility Mapping Using Genetic Algorithm. *Eng. Geol.* **2015**, *192*, 101–112. [CrossRef]

60. Pacheco Quevedo, R.; Velastegui-Montoya, A.; Montalván-Burbano, N.; Morante-Carballo, F.; Korup, O.; Daleles Rennó, C. Land Use and Land Cover as a Conditioning Factor in Landslide Susceptibility: A Literature Review. *Landslides* **2023**, *20*, 967–982. [CrossRef]
61. Wen, H.; Song, C.; Xiang, X.; Xiong, F. Optical Remote Sensing Change Detection Method for the Identification of Landslide Clusters Induced by Heavy Rainfall. *Sci. Surv. Mapp.* **2022**, *47*, 193–202. [CrossRef]
62. Chen, C.; Fan, L. Selection of Contributing Factors for Predicting Landslide Susceptibility Using Machine Learning and Deep Learning Models. *Stoch. Environ. Res. Risk Assess.* **2023**, 1–26. [CrossRef]
63. Yu, H.; Pei, W.; Zhang, J.; Chen, G. Landslide Susceptibility Mapping and Driving Mechanisms in a Vulnerable Region Based on Multiple Machine Learning Models. *Remote Sens.* **2023**, *15*, 1886. [CrossRef]
64. Yang, J.; El-Kassaby, Y.A.; Guan, W. The Effect of Slope Aspect on Vegetation Attributes in a Mountainous Dry Valley, Southwest China. *Sci. Rep.* **2020**, *10*, 16465. [CrossRef] [PubMed]
65. Donnarumma, A.; Revellino, P.; Grelle, G.; Guadagno, F.M. Slope Angle as Indicator Parameter of Landslide Susceptibility in a Geologically Complex Area. In *Landslide Science and Practice: Volume 1: Landslide Inventory and Susceptibility and Hazard Zoning*; Margottini, C., Canuti, P., Sassa, K., Eds.; Springer: Berlin/Heidelberg, Germany, 2013; pp. 425–433.
66. Sabzevari, T.; Noroozpour, S.; Pishvaei, M.H. Effects of Geometry on Runoff Time Characteristics and Time-Area Histogram of Hillslopes. *J. Hydrol.* **2015**, *531*, 638–648. [CrossRef]
67. Amatulli, G.; McInerney, D.; Sethi, T.; Strobl, P.; Domisch, S. Geomorpho90m: Empirical Evaluation and Accuracy Assessment of Global High-Resolution Geomorphometric Layers. *Sci. Data* **2020**, *7*, 162. [CrossRef] [PubMed]
68. Moore, I.D.; Burch, G.J. Physical Basis of the Length-Slope Factor in the Universal Soil Loss Equation. *Soil. Sci. Soc. Am. J.* **1986**, *50*, 1294–1298. [CrossRef]
69. Chowdhury, M.S. Modelling Hydrological Factors from DEM Using GIS. *MethodsX* **2023**, *10*, 102062. [CrossRef]
70. Mockler, E.M.; O'Loughlin, F.E.; Bruen, M. Understanding Hydrological Flow Paths in Conceptual Catchment Models Using Uncertainty and Sensitivity Analysis. *Comput. Geosci.* **2016**, *90*, 66–77. [CrossRef]
71. Yu, X.; Zhang, K.; Song, Y.; Jiang, W.; Zhou, J. Study on landslide susceptibility mapping based on rock–soil characteristic factors. *Sci. Rep.* **2021**, *11*, 15476. [CrossRef]
72. Chen, L.; Guo, H.; Gong, P.; Yang, Y.; Zuo, Z.; Gu, M. Landslide Susceptibility Assessment Using Weights-of-Evidence Model and Cluster Analysis Along the Highways in the Hubei Section of the Three Gorges Reservoir Area. *Comput. Geosci.* **2021**, *156*, 104899. [CrossRef]
73. Bopche, L.; Rege, P.P. Landslide Susceptibility Mapping: An Integrated Approach Using Geographic Information Value, Remote Sensing, and Weight of Evidence Method. *Geotech. Geol. Eng.* **2022**, *40*, 2935–2947. [CrossRef]
74. Ilia, I.; Tsangaratos, P. Applying weight of evidence method and sensitivity analysis to produce a landslide susceptibility map. *Landslides* **2016**, *13*, 379–397. [CrossRef]
75. Regmi, N.R.; Giardino, J.R.; Vitek, J.D. Modeling Susceptibility to Landslides Using the Weight of Evidence Approach: Western Colorado, USA. *Geomorphology* **2010**, *115*, 172–187. [CrossRef]
76. Neuhauser, B.; Damm, B.; Terhorst, B. GIS-Based Assessment of Landslide Susceptibility on the Base of the Weights-of-Evidence Model. *Landslides* **2012**, *9*, 511–528. [CrossRef]
77. Ayalew, L.; Yamagishi, H.; Ugawa, N. Landslide Susceptibility Mapping Using GIS-Based Weighted Linear Combination: The Case in Tsugawa Area of Agano River, Niigata Prefecture, Japan. *Landslides* **2004**, *1*, 73–81. [CrossRef]
78. Bonham-Carter, G.F. *Geographic Information Systems for Geoscientists: Modelling with GIS*; Computer Methods in the Geosciences; Pergamon Press: Oxford, UK, 1994; Volume 13, p. 398.
79. Bonham-Carter, G.F.; Agterberg, F.P.; Wright, D.F. Weights of Evidence Modelling: A New Approach to Mapping Mineral Potential. In *Statistical Applications in the Earth Sciences*; Agterberg, F.P., Bonham-Carter, G.F., Eds.; Geological Survey of Canada, Paper 89–9; Geological Survey of Canada: Ottawa, ON, Canada, 1989; pp. 171–183.
80. Barbieri, G.; Cambuli, P. The Weight of Evidence Statistical Method in Landslide Susceptibility Mapping of the Rio Pardu Valley (Sardinia, Italy). In Proceedings of the 18th World IMACS/MODSIM Congress, Cairns, Australia, 13–17 July 2009; pp. 13–17.
81. Can, T.; Nefeslioglu, H.A.; Gokceoglu, C.; Sonmez, H.; Duman, T.Y. Susceptibility Assessments of Shallow Earthflows Trig-gered by Heavy Rainfall at Three Catchments by Logistic Regression Analysis. *Geomorphology* **2005**, *72*, 250–271. [CrossRef]
82. Pradhan, B.; Lee, S. Regional Landslide Susceptibility Analysis Using Back-Propagation Neural Network Model at Cameron Highlands, Malaysia. *Landslides* **2010**, *7*, 13–30. [CrossRef]
83. Alembante, G.; Meten, M. Landslide Susceptibility Mapping Using GIS-Based Information Value and Frequency Ratio Methods in Gindeberet Area, West Shewa Zone, Oromia Region, Ethiopia. *Res. Sq.* **2021**. [CrossRef]
84. Chung, C.J.F.; Fabbri, A.G. Probabilistic Prediction Models for Landslide Hazard Mapping. *Photogramm. Eng. Remote Sens.* **1999**, *65*, 1389–1399.
85. Chung, C.J.F.; Fabbri, A.G. Validation of Spatial Prediction Models for Landslide Hazard Mapping. *Nat. Hazards* **2003**, *30*, 451–472. [CrossRef]

86. Guzzetti, F.; Reichenbach, P.; Cardinali, M.; Galli, M.; Ardizzone, F. Probabilistic landslide hazard assessment at the basin scale. *Geomorphology* **2005**, *72*, 272–299. [CrossRef]
87. Chapi, K.; Singh, V.P.; Shirzadi, A.; Shahabi, H.; Bui, D.T.; Pham, B.T.; Khosravi, K. A Novel Hybrid Artificial Intelligence Approach for Flood Susceptibility Assessment. *Environ. Model. Softw.* **2017**, *95*, 229–245. [CrossRef]
88. ESRI. *ArcGIS Desktop: Release 10.5*; Environmental Systems Research Institute: Redlands, CA, USA, 2015; Available online: https://desktop.arcgis.com/en/index.html (accessed on 18 November 2024).
89. Agboola, G.; Hashemi Beni, L.; Elbayoumi, T.; Thompson, G. Optimizing landslide susceptibility mapping using machine learning and geospatial techniques. *Ecol. Inform.* **2024**, *81*, 102583. [CrossRef]
90. Feddema, J.J. A Revised Thornthwaite-Type Global Climate Classification. *Phys. Geogr.* **2005**, *26*, 442–466. [CrossRef]
91. Mountrakis, D.M. *Geology and Tectonic Evolution of Greece*, 1st ed.; University Studio Press: Thessaloniki, Greece, 2010; p. 373. ISBN 978-960-12-1970-7.
92. I.G.M.E. *Geological Map of Greece, Scale 1:50,000—Zagora-Siki Sheet*; Institute of Geological and Mineral Exploration: Athens, Greece, 2013.
93. He, K.; Yang, Q.; Shen, X.; Dimitriou, E.; Mentzafou, A.; Papadaki, C.; Stoumboudi, M.; Anagnostou, E.N. Brief Communication: Storm Daniel Flood Impact in Greece in 2023: Mapping Crop and Livestock Exposure from Synthetic-Aperture Radar (SAR). *Nat. Hazards Earth Syst. Sci.* **2024**, *24*, 2375–2382. [CrossRef]
94. Huffman, G.J.; Stocker, E.F.; Bolvin, D.T.; Nelkin, E.J.; Tan, J. *GPM IMERG Final Precipitation L3 Half Hourly 0.1 Degree × 0.1 Degree*; V06; Goddard Earth Sciences Data and Information Services Center (GES DISC): Greenbelt, MD, USA, 2019. [CrossRef]
95. Ray, R.L.; Lazzari, M.; Olutimehin, T. Remote Sensing Approaches and Related Techniques to Map and Study Landslides. *Landslides-Investig. Monit.* **2020**, *2*, 1–25.
96. Singh, P.; Maurya, V.; Dwivedi, R. Pixel Based Landslide Identification Using Landsat 8 and GEE. In Proceedings of the 2021 IEEE International Geoscience and Remote Sensing Symposium IGARSS, Brussels, Belgium, 11–16 July 2021; pp. 8444–8447. [CrossRef]